LBL-2848
c.2

POSITRON EMISSION CAMERA FOR TRANSVERSE SECTION TOMOGRAPHY

Stephen E. Derenzo, Haim Zaklad, and Thomas F. Budinger

DONNER LABORATORY

December 1975

Prepared for the U. S. Energy Research and Development Administration under Contract W-7405-ENG-48

TWO-WEEK LOAN COPY

This is a Library Circulating Copy which may be borrowed for two weeks. For a personal retention copy, call Tech. Info. Division, Ext. 5716

LAWRENCE BERKELEY LABORATORY • UNIVERSITY OF CALIFORNIA • BERKELEY

48

LBL-2848
c.2

DISCLAIMER

This document was prepared as an account of work sponsored by the United States Government. While this document is believed to contain correct information, neither the United States Government nor any agency thereof, nor the Regents of the University of California, nor any of their employees, makes any warranty, express or implied, or assumes any legal responsibility for the accuracy, completeness, or usefulness of any information, apparatus, product, or process disclosed, or represents that its use would not infringe privately owned rights. Reference herein to any specific commercial product, process, or service by its trade name, trademark, manufacturer, or otherwise, does not necessarily constitute or imply its endorsement, recommendation, or favoring by the United States Government or any agency thereof, or the Regents of the University of California. The views and opinions of authors expressed herein do not necessarily state or reflect those of the United States Government or any agency thereof or the Regents of the University of California.

CONTENTS

ABSTRACT iii

1. INTRODUCTION 1

2. BACKGROUND 3

3. RATIONALE

3.1 Myocardial Accumulation of Rubidium. 11

3.2 Need for Multiple Views or Equivalent Imaging. 11

3.3 Positron Mode Imaging Rationale. 12

3.4 Choice of Isotope. 13

3.5 Rationale for Geometry and Data Handling Configuration 14

4. PHYSICAL DESCRIPTION OF THE SYSTEM 19

4.1 Shielding. 21

4.2 Choice of NaI(Tl) Crystals 25

4.3 Crystal Position Coding. 25

4.4 Energy and Time Resolution 26

4.5 Readout. 28

4.6 Attenuation Corrections. 29

5. PROPERTIES OF THE SYSTEM FOR THE DETECTION OF COINCIDENT ANNIHILATION RADIATION

5.1 Crystal Detection Efficiency 30

5.2 Axial Response Function. 30

5.3 Sensitivity. 33

5.4 Effect of the Range of Positrons in Tissue . . 36

5.5 Effect of Deviations from 180° Line of Flight. 36

5.6 Transaxial Resolution Function 37

5.7 Shielding and Backgrounds. 41

5.8 Deadtime 55

1. INTRODUCTION

We propose an imaging device for the rapid, non-invasive, high resolution (6 mm FWHM), three-dimensional reconstruction of the myocardium in end-systole and end-diastole. The instrument can also be used for transverse axial tomography of the head and abdomen. The major emphasis is to image the accumulation of ^{82}Rb (positron emitter) in the myocardium after i.v. injection. This isotope has a 75-sec half-life, and can be readily obtained from a portable generator containing ^{82}Sr, which decays to ^{82}Rb with a 25-day half-life. Studies of blood flow are also feasible using ^{68}Ga or ^{82}Rb. The device we have designed incorporates multiple crystals in a ring and a data collection scheme based on coded light pipes. Transverse tomography of body sections from 5 to 15 mm thick are imaged in 1 to 5 min without rotation. Both transmission and emission modes are envisioned in order to effect compensation for attenuation in quantitative studies and comparison of anatomy to function using algorithms already developed.

More than 100,000 Americans die each year from fatal heart attacks. An essential aspect of prevention is early diagnosis and understanding of the pathophysiologic processes in the myocardium. The instrument we propose presents a method for the non-invasive study of myocardial disease associated with diminution in flow. The instrument also allows the rapid assessment of dyskinesia and can be used in conjunction with a number of isotopes but is basically for use with short half life positron emitters. Good examples are

Rubidium^{82} and Galium^{68} which can be obtained from a generator remote from a cyclotron. ^{18}F for imaging acute myocardial infarctions is another important application. This device has the potential for imaging not only the heart in end-systole and end-diastole, but for assessing brain flow with 10 second frame times and for imaging distribution of isotopes or density (5% accuracy) in other organs such as the pancreas, prostate, and bladder.

2. BACKGROUND

Early studies by Love and Burch (1957) with Rubidium-86 and Carr and co-workers (1964) with ^{131}Cs suggested that these alkaline metals are extracted by the myocardium in much the same way as potassium, and can be used to infer coronary flow in accordance with the Sapirstein principle (Sapirstein, 1958). In the past four years there has been an intense effort to develop noninvasive techniques for delineating normal or abnormal myocardial perfusion using the radionuclides of potassium, rubidium, and cesium as well as coronary injection techniques using labeled albumin or particle microspheres and xenon. The background work in assessing coronary flow and myocardial functional integrity is shown in Table 1.

These efforts, while notable for establishment of the clinical efficacy of imaging the myocardial accumulation of isotopes, have not given us a substantially useful tool for noninvasive evaluation of coronary flow or myocardial integrity. The reason appears not to be in the selection of isotope so much as in the instrumentation for gated three-dimensional distribution delineation. Our previous work with the positron emitter ^{82}Rb (Budinger, Yano and Hoop, 1975; and Volkelman et al., 1972) suggests that this isotope given in 3-5 mCi amounts can provide sufficient data for transverse section reconstruction of the human heart in gated studies. Previous work in instrumentation for three-dimensional imaging of nuclide distribution has been limited to the head. This work has been with a rectilinear scanner (Kuhl and Edwards, 1963; Kuhl and Edwards, 1968; Kuhl et al., 1973)

and some studies with phantoms and patients have been made with the gamma camera (Budinger et al., 1974). Recently using ^{129}Cs, we have been able to image transverse sections of the human myocardium (Fig. 1) and the myocardium of the dog (Fig. 2). The reconstruction of transverse sections was carried out using five different algorithms and six methods for the compensation of attenuation were incorporated in these and other studies (Budinger and Gullberg, 1974). These studies done with the gamma scintillation camera are inadequate because of low statistics, and clumsy patient rotation schemes (many have been explored). Using ^{81}Rb, we explored the feasibility of gating studies of the myocardium (see Fig. 3) with good results with one view; however, we have not yet combined gating with multiple views due to lack of adequate parallel hole collimation for the 450 - 520 keV photons of ^{81}Rb and the 600 - 1400 keV emmanations of ^{82m}Rb contamination present in some preparations.

This problem might be overcome by use of lower energy nuclides such as ^{201}Tl, which just now is becoming available (Lebowitz et al., 1974). However, this isotope has a 75-hr half-life, and does not provide the characteristics of a positron emitter for transverse section imaging.

Even the best spatial resolution imaging device cannot give in one view a satisfactory representation of the three-dimensional distribution of the isotopes. While tomographic imaging can be accomplished using a moving, focusing collimator (Anger, 1968; Mathieu and Budinger, 1974), or a coded aperture technique (Barrett et al., 1973; Chan et al., 1974; Budinger and Macdonald, 1975),

HUMAN MYOCARDIUM TRANSVERSE SECTIONS

Tc-99m
TRANSMISSION

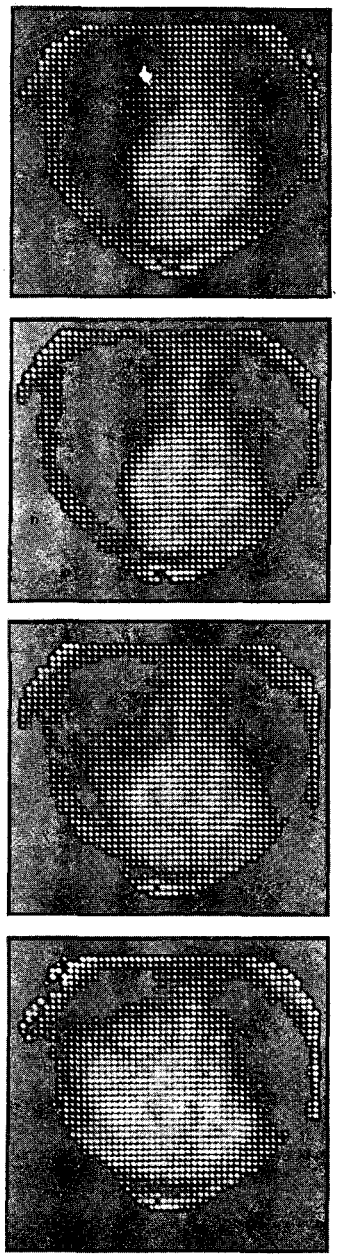

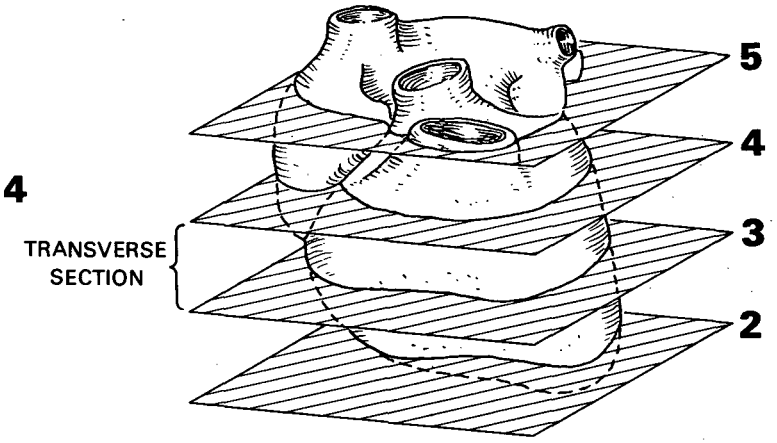

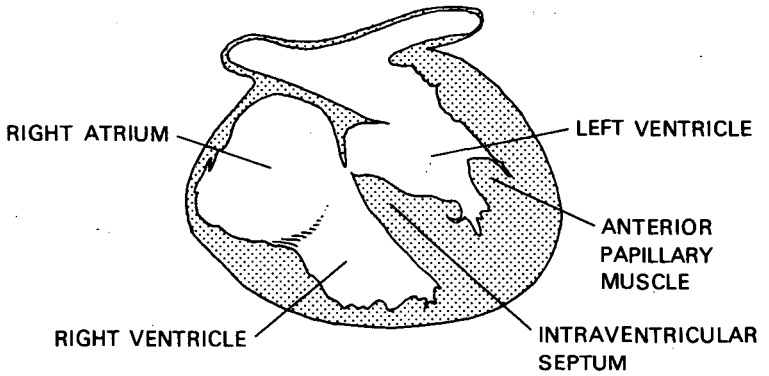

Cs-129
EMISSION CORRECTED
FOR TRANSMISSION

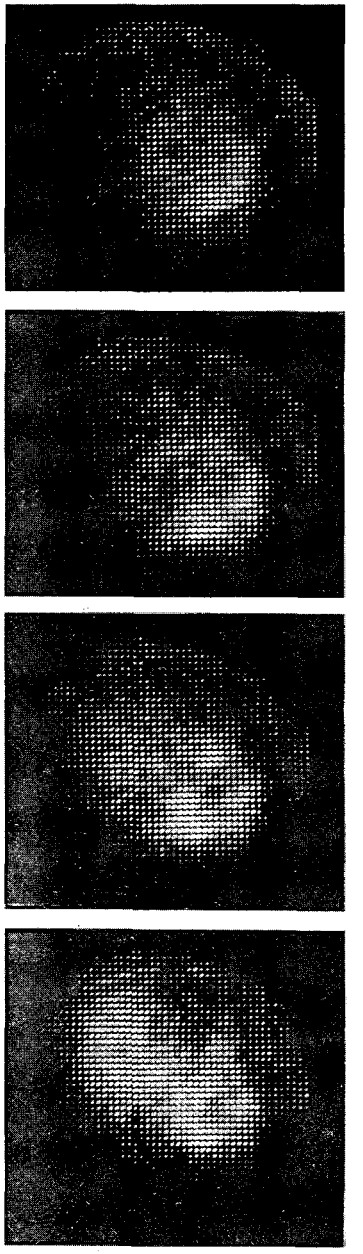

Fig. 1

XBB 749-6039

DOG MYOCARDIUM
TRANSVERSE SECTION RECONSTRUCTION

TRANSMISSION	EMISSION	
Tc-99m	Se-75 METHIONINE	
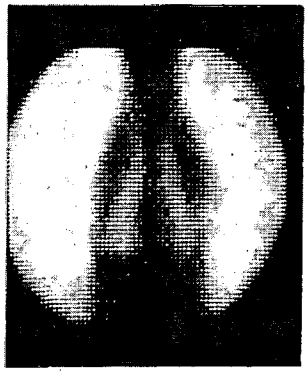	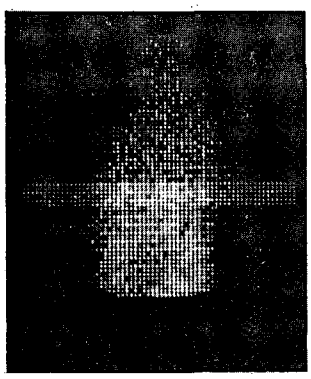	PROJECTION
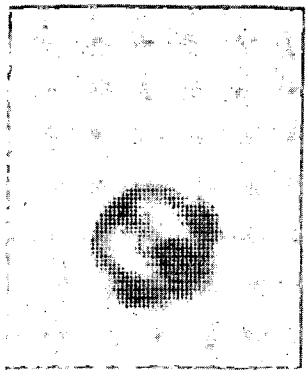	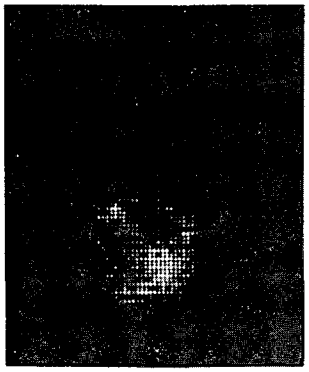	TRANSVERSE SECTION

XBB 748-4532A

Fig. 2

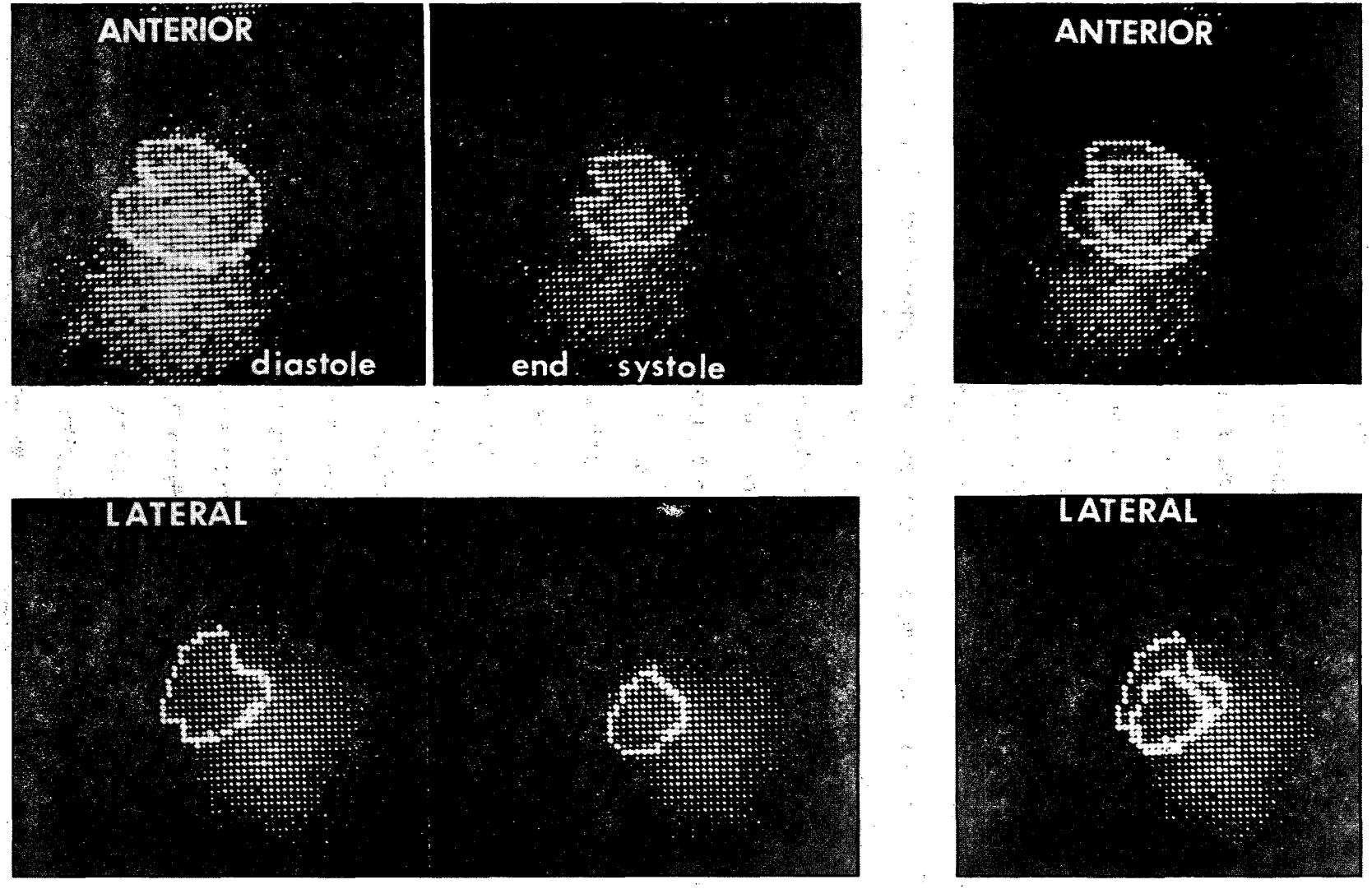

XBB 745-3465

Fig. 3

the result is an image of the plane of interest with continuous planes superposed as a heterogeneous out-of-focus background.

A positron camera can be used in a fashion which allows focusing on one plane (Brownell and Burnham, 1972); however, the adjacent planes will also be present in the image, but out of focus. This type of imaging selected planes with the positron camera is equivalent to back projection or simple superposition.

The Brownell camera at Massachusetts General Hospital has been used for transverse section imaging on phantoms and dogs with good results (Chesler, 1973). These studies involve rotation of the subject between the camera planes. Thus multiple injections are required for sufficient data due to the short half-life of the positron emitters $^{13}NH_3$, ^{82}Rb, and ^{38}K.

The Anger positron camera, employing a scintillation camera in coincidence with a crystal array, has been in operation for a number of years, but the count rate limitations (~ 1000 sec^{-1}) obviate its usefulness for the studies we envision.

A positron camera employing two gas-filled multiwire proportional chambers is being developed at the University of California San Francisco Medical Center and Lawrence Berkeley Laboratory. This system uses lead honeycomb converters and each of the two detector planes has efficiencies from 2.5% to 10% depending upon the number of chambers and converters used. The coincidence rate in air is 330 events per sec. (30-μCi source) (10% accidentals). The spatial resolution is 6-7 mm FWHM (Lim et al., 1975). No collimation is provided

and energy selection is not possible. It appears that in a 20-cm cylinder of tissue, approximately 70% of the coincident events will not provide useful spatial information (Derenzo, 1975).

Another two-plane positron camera system employing two Anger scintillation cameras is being developed at Searle Radiographics, Inc. (Muehllehner, 1975). The resolution is 10 mm FWHM and counting rates in excess of 4000 sec^{-1} are possible in 12 cm water.

Efficient transaxial tomography using the above systems involves patient or detector rotation, and dynamic flow studies are not possible except indirectly through use of the equilibrium image method proposed by Brownell, Ter-Pogossian and others (Jones et al., 1974).

Ring detector systems have been built for positron mode transverse section imaging. Studies are underway at Brookhaven National Laboratory using a 32-detector ring which is 40 cm in diameter. Each detector is a NaI(Tl) crystal of 3.2 cm diameter (Robertson et al., 1973). The resolution and sensitivity of this innovative device are limited by the large size and small number of crystals.

At the Washington University School of Medicine a ring of detectors has been built for positron imaging and transverse section tomography (Ter-Pogossian et al., 1975; Phelps et al., 1975). The device at present is a hexagonal ring of 48 NaI(Tl) detectors, each 5 cm × 5 cm diameter. Preliminary work demonstrates excellent depth insensitivity, quantitative image reconstruction, good contrast, and 14 mm FWHM image resolution. The detectors were stopped down to 2.5 cm diameter in order to achieve this resolution, resulting in a

loss in sensitivity. Gated imaging might be difficult because of the need to rotate the apparatus through many positions for every section to be imaged.

In summary, previous work using various radiopharmaceuticals and imaging devices for assessing the integrity of the human myocardium have laid the important ground work for the device we propose here. We wish to construct a device capable of performing rapid, high resolution images of the heart. In addition this device has application to head and abdomen, without modification.

3. RATIONALE

3.1 Myocardial Accumulation of Rubidium. The overall objective of ascertaining myocardial perfusion by the accumulation of rubidium involves a basic assumption that the amount of nuclide present in the muscle is directly proportional to the flow. This principle (Sapirstein, 1956, 1958) asserts that the fraction of isotope present in each organ is directly related to the fraction of cardiac output that organ receives. This is true to a first approximation for potassium, rubidium, and $^{13}NH_3$ where the extraction efficiency is high, and the Sapirstein principle can yield valuable clinical data if we have some means of reaching inside the myocardium to make analyses. The problem is that we can only estimate the isotope concentration because what is normally imaged is a projection of the three-dimensional distribution on a two-dimensional plane. The distribution of isotope in the wall as well as its gradient through the wall are important clinical observations for which there exists no in vivo techniques (Yipintsoi et al., 1973).

3.2 Need for Multiple Views or Equivalent Imaging. Activity in under- and overlying tissues is superimposed on the myocardial activity and results in poor contrast for single view images; that is, the target-to-nontarget ratio in the object is reduced from a true ratio of 7:1 to less than 2:1 in the projected image. For positive imaging of infarctions using ^{99m}Tc-tetracycline or ^{99m}Tc-pyrophosphate, the situation is not as serious because the true ratios are closer to 12:1 and 20:1, respectively. Yet even with these latter radiopharmaceuticals,

methods of avoiding the superposition of rib and sternum activity are most important, and multiple views are needed for quantitative data.

Another reason for the desirability of heart transverse sections is to quantitate the amount of isotope present in order to grade the quantity of accumulated isotope. Using ^{81}Rb, which has both positron annihilation gammas and 190 keV photons from ^{81m}Kr, it is possible to measure flow by examining the ratio of Rb to Kr. A high ratio indicates relatively greater flow over a low ratio. Our previous experience with this isotope has led to inconsistent results, probably due to the accumulation in the lungs. Transverse section imaging would avoid this problem.

Thus, there are four reasons for going to the design and instrumentation given here:

1. Selectively remove background from under- and overlying tissue.
2. Aid in detection of intramyocardial defect by transverse section display of data.
3. Provide a quantitative method of assessing the concentration of isotope of a μCi per gram basis.
4. Provide a means for evaluating nuclide flow into and out of the myocardium.

3.3 Positron Mode Imaging Rationale. A severe limitation in nuclide imaging has been the very low statistics. The data are limited by the dose to the patient and instrument performance. Whereas, millicurie amounts (3.7×10^7 disintegrations per sec) are injected, the presence of scattering and very poor transmission of collimators (3×10^{-4} to 3×10^{-5} for isotopes of interest) leave us with little data to work with, particularly in the beating heart where image motion requires

ten times more disintegrations than for no motion imaging. An analysis of this situation leads to the conclusion that in order to achieve our objective, we must get rid of the collimator and use an isotope with a very short half-life to reduce the dose. Positron mode imaging is clearly the answer, and ^{38}K, ^{81}Rb, and $^{13}NH_3$ are already proven isotopes.

3.4 Choice of Isotope. Radionuclides of the chemically related alkaline elements potassium, rubidium, and cesium and their analogs have been shown to be of clinical value in the direct assessment of the distribution of myocardial blood flow using noninvasive scintigraphic techniques. High resolution positron scintigraphic techniques appear particularly attractive not only for localization and sizing of myocardial infarctions, but for direct assessment of the distribution of regional myocardial blood flow.

However, of the many radioisotopes of potassium analogs, relatively few are positron emitters. Among these are: ^{38}K, 7.7 min; ^{79}Rb, 21 min; ^{81}Rb, 4.6 hr; ^{82}Rb, 1.2 min; ^{82m}Rb, 6.3 hr; ^{84}Rb, 33 d; and ^{13}N-ammonia, 10 min. Of these nuclides, ^{79}Rb, ^{82}Rb, and ^{13}N-ammonia are relatively free from other gamma rays and are sufficiently short lived to be useful in acute clinical situations in which the patient's condition is changing rapidly, thus enabling repeated studies particularly to assess the efficacy of various modes of therapy. Studies using most of these radionuclides require a charged-particle accelerator near the hospital or clinic. An exception is ^{82}Rb, which can be obtained from a long-lived ^{82}Sr generator (25-d half-life) and is therefore available,

at will, for application in acute clinical situations. In addition, its short half-life offers low radiation exposure to the patient (Budinger, et al., 1974) (Fig. 4).

Both ^{82}Rb and ^{68}Ga (available from 280D ^{68}Ge) can be used to delineate hemodynamic flow through the heart chambers and the brain. ^{68}Ga is suitable because of its 68 min half-life and availability as a chelate with EDTA. In this form it will remain in the intravascular space.

3.5 Rationale for Geometry and Data Handling Configuration. Previous attempts to image positrons dating from 1951 (Wrenn, et al. 1951, and Brownell and Sweet, 1953) have been somewhat limited by detector saturation. Camera devices also saturate at count rates below those needed for adequate data gathering. This is certainly the case for the Anger positron camera whose efficiency in air is ~ 30 cts sec^{-1} μCi^{-1}, but only about 250 μCi can be in the field of view at one time.

The MGH camera (Burnham et al., 1972) can tolerate 3 mCi or more, and has been used to give good myocardial images with ^{82}Rb (Budinger et al., 1974).

Our approach is to examine all the way around the heart at one time, with a ring of 288 crystals (Figs. 5 & 6). A section 5 to 15 mm thick will be imaged on each injection.

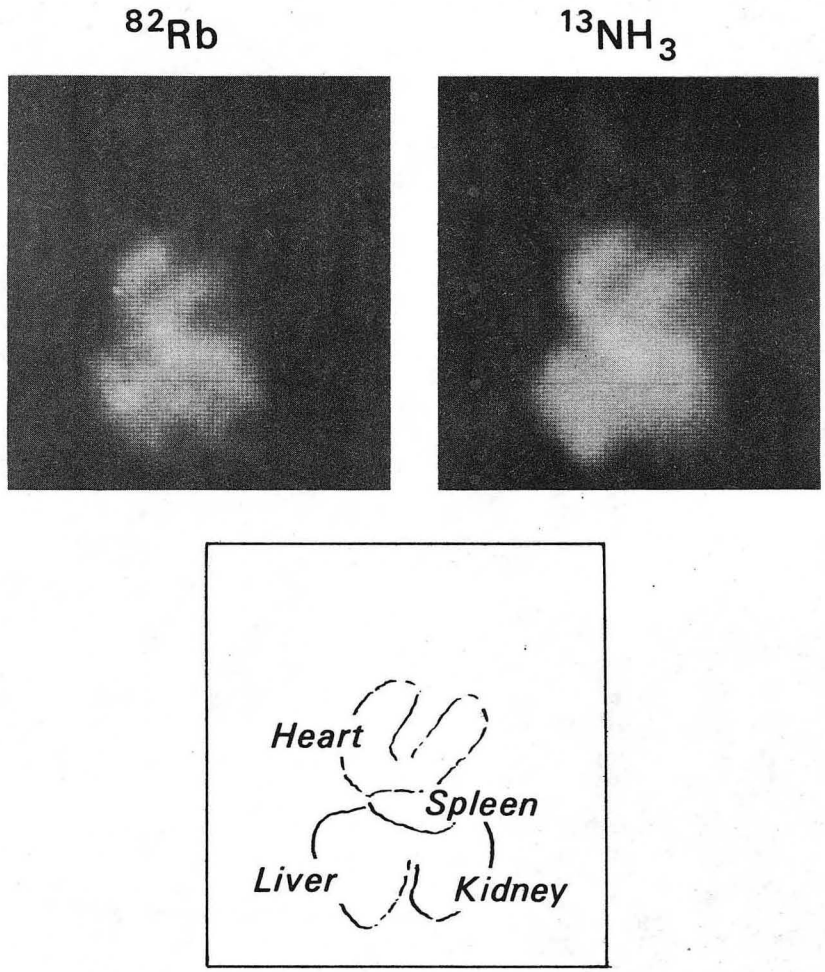

XBB 746-4132

Fig. 4

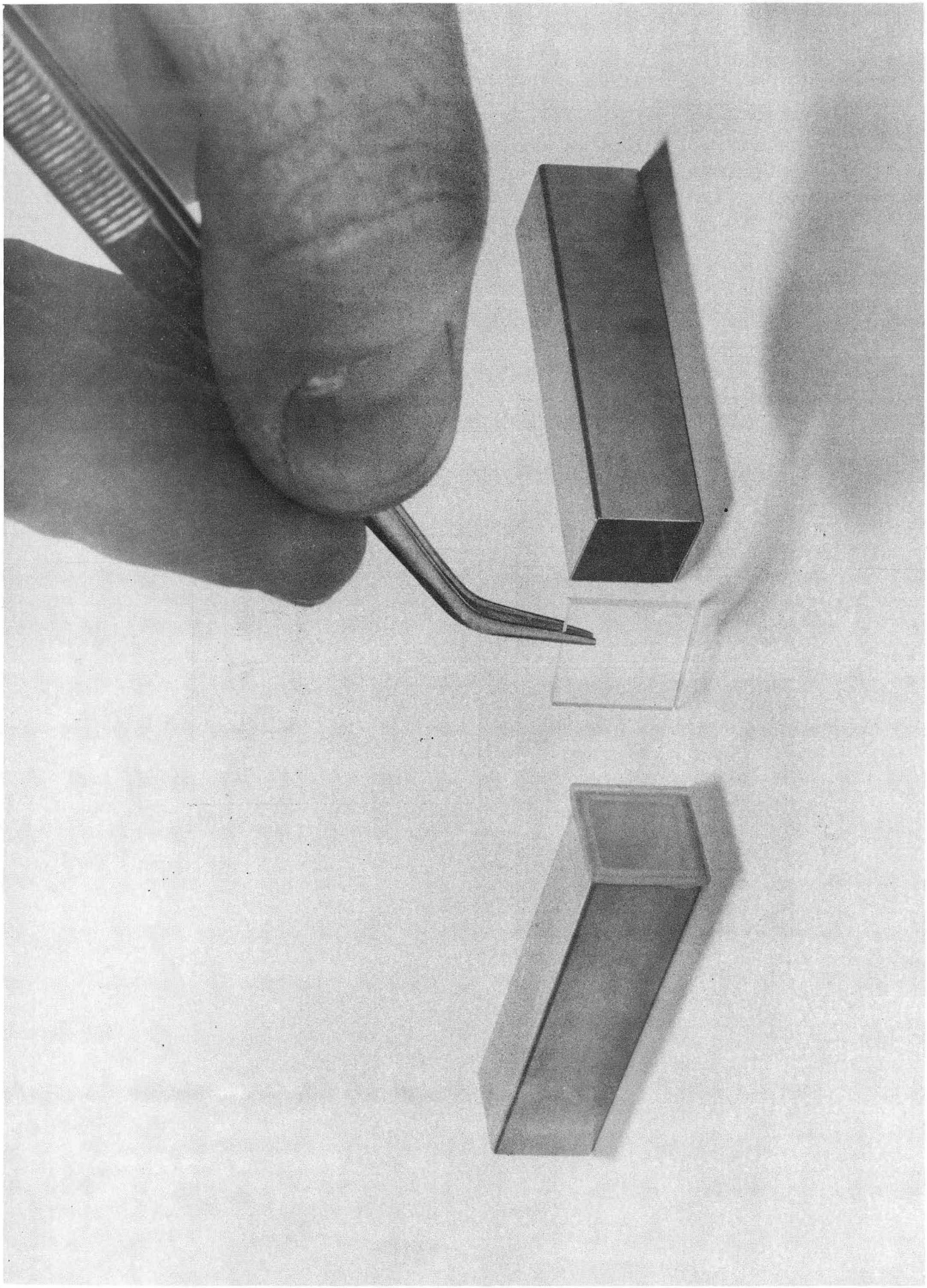

XBB 749-6340

Fig. 5

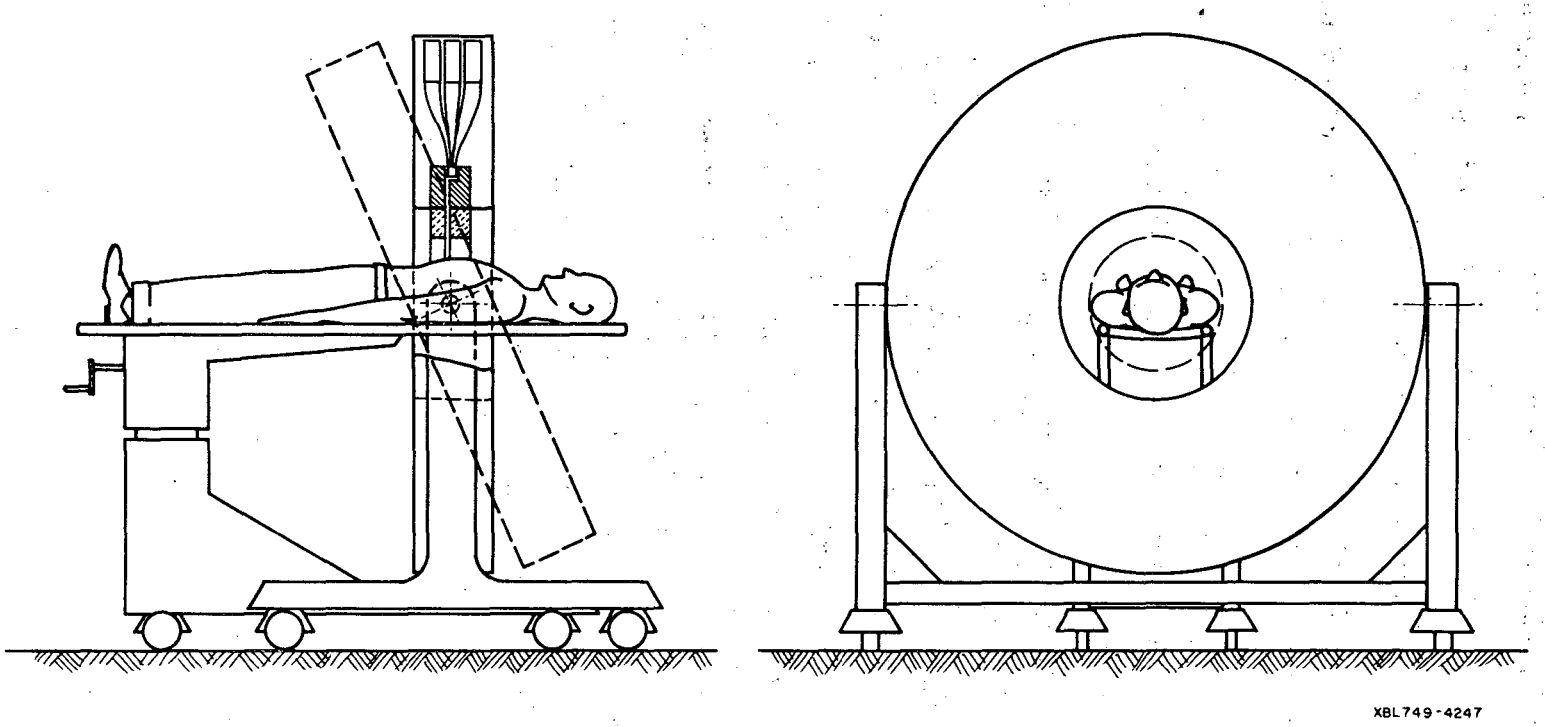

Fig. 6

In order to achieve adequate statistics to present a transverse image of the myocardium after a single injection of ^{82}Rb (75 sec half-life), we envision the following:

(a) the heart is 10 cm in the cephlad-caudad dimension, and the myocardial volume is 150 cm^3;

(b) the cardiac rate is 72 min^{-1};

(c) the scattering medium is equivalent to a 20 cm diam cylinder of water;

(d) 20 mCi of ^{82}Rb is injected i.v. and 3.5% of this is extracted by the myocardium;

(e) eight separate images are taken, each corresponding to a 0.1 sec interval of the 0.8 sec cardiac cycle;

(f) data are taken for a period of 200 sec after an initial 100 sec wait for the blood pool clearance of ^{82}Rb;

(g) as in Table 3, Case I, the imaging sensitivity is 31 events sec^{-1} [μCi per axial cm]$^{-1}$. The resulting initial activity density is 0.7 μCi per 4 × 4 × 10 mm image element and for each of the eight images typically 100 events will be collected per image element.

4. PHYSICAL DESCRIPTION OF THE SYSTEM

The patient is positioned on a specially designed bed that can be inserted into the ring detector (Fig. 6). The bed can be adjusted vertically and is cantilevered from one end. The other end in the field of view of the detector is made to minimize interaction with the gamma rays. (Thin aluminum tubes and canvas back.) The overall dimension of the ring assembly is 170 cm OD and 60 cm ID, and an additional insert can be used to reduce the backgrounds by reducing the ID to 40 cm. The assembly can be tilted 20° from the vertical to allow for an oblique view of the heart.

The detector consists of an array of NaI(Tl) crystals measuring 0.8 cm wide × 3 cm high × 5 cm deep mounted in a ring 80 cm in diameter (Fig. 7). The total number of crystals is 288. The ring is broken into 8 segments of 36 crystals each. Lead shielding is mounted on the inner circle of the detector extending inward to a diameter of 60 cm. An additional collimator (typically 40 cm ID) is shown in broken lines.

A source containing ^{133}Ba (not shown) is mounted on a rail inside the collimator opening and driven by a motor. The source generates a 60° fan beam, and travels 180° of the periphery. The position of the source is digitized and the counts collected by the detecting crystals are stored for a subsequent computation of the attenuation distribution in the section.

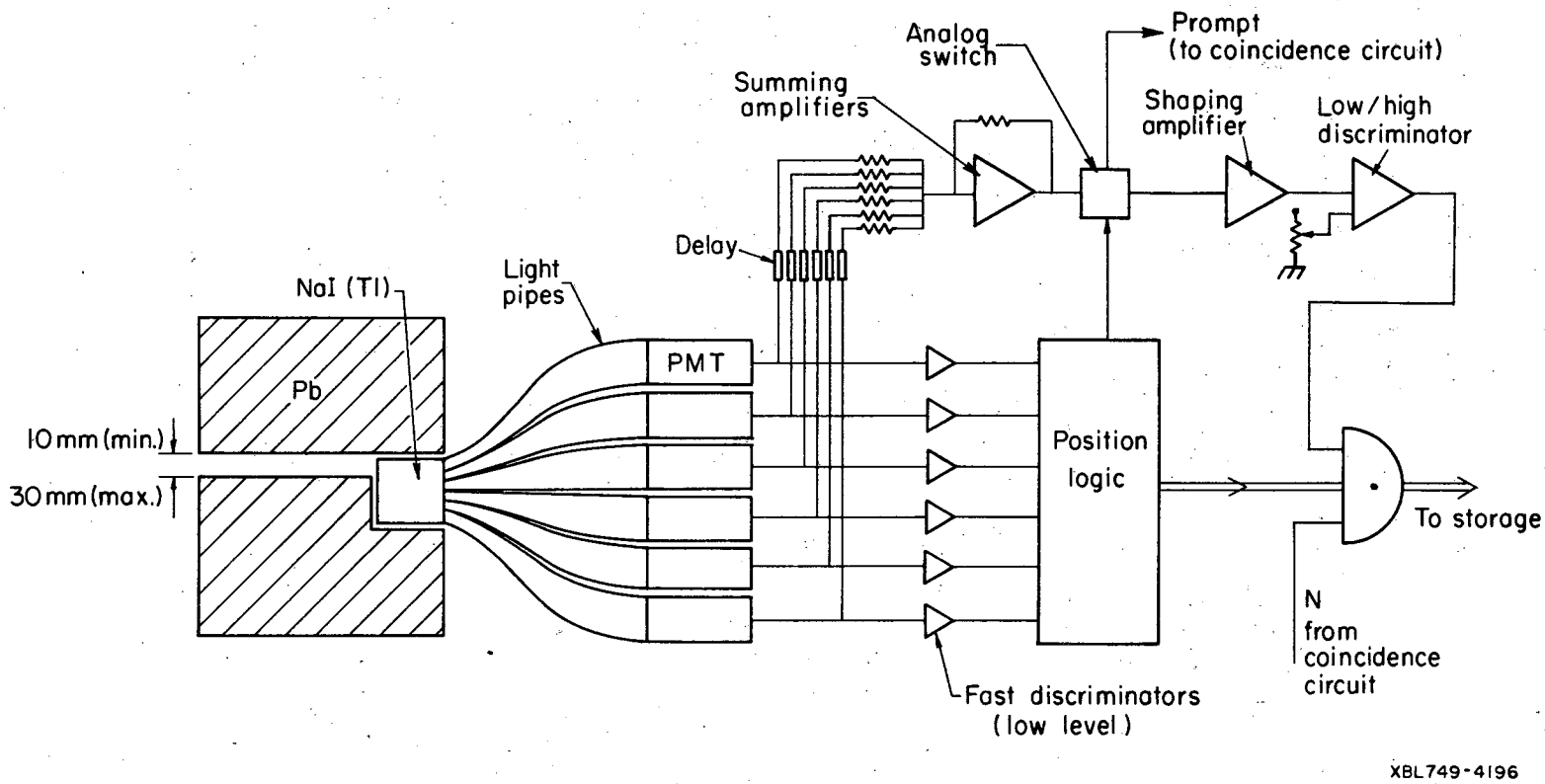
Analog switch
Prompt (to coincidence circuit)
Summing amplifiers
Shaping amplifier
Low/high discriminator
Delay
Light pipes
NaI (Tl)
PMT
Pb
10 mm (min.)
30 mm (max.)
Position logic
To storage
N from coincidence circuit
Fast discriminators (low level)
XBL749-4196

Fig. 7

Co-linear gamma rays due to positron annihilation in the patient scintillate in NaI crystals. Light generated in a crystal exits into coded light-pipes (example in Fig. 8). Nine photomultipliers per segment view this decoding network utilizing a specially designed code to generate a binary word corresponding to the position. A coincidence circuit (example in Fig. 9) checks for coincidence between any crystal and the opposing 62 crystals. This allows a possibility of 8,928 coincident crystal pairs and provides a nearly uniform geometrical sensitivity over the central 30 cm. If coincidence has been found, the sum of the PMT outputs is energy selected and the data is transferred to storage. The stored positional information is processed using a three-dimensional reconstruction program that corrects for the attenuation in the tissue (generated by the traveling source) to reconstruct an image of the section.

4.1 Shielding. The purpose of the lead shielding is two-fold:

1. Provide a mechanism for varying the slice thickness.
2. Absorb gammas originating from tissue external to the field of view.

The shield consists of two concentric rings extending over the crystal ring with an OD = 106 cm and ID = 40 cm; this determines the slice thickness (see Fig. 10). The internal diameter of 40 cm can be varied by removing a part of the assembly and inserting an alternate to fit different patient sizes.

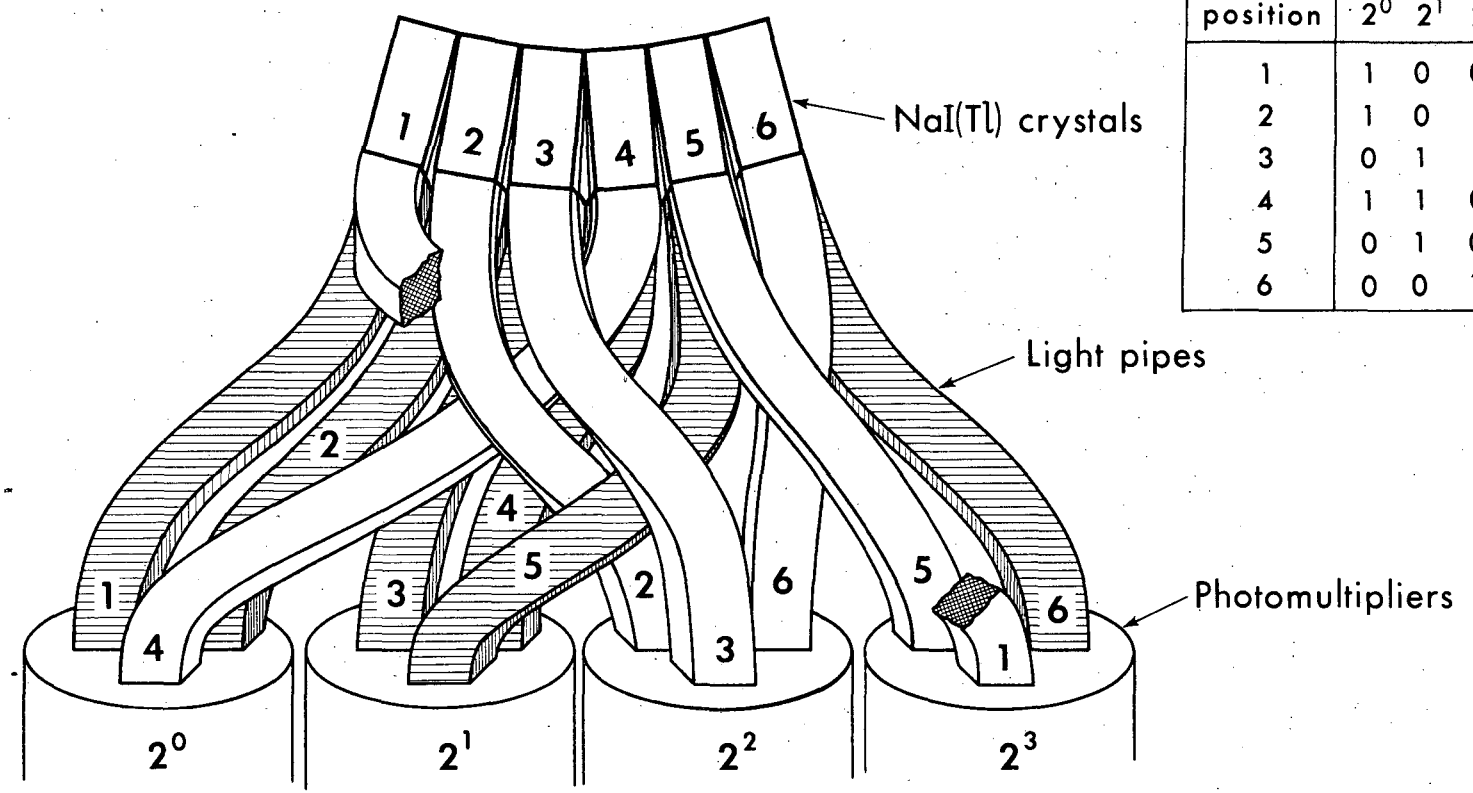

Light Pipe Connection Scheme

Crystal position	PMT 2^0	2^1	2^2	2^3
1	1	0	0	1
2	1	0	1	0
3	0	1	1	0
4	1	1	0	0
5	0	1	0	1
6	0	0	1	1

XBL 757-3460

Fig. 8

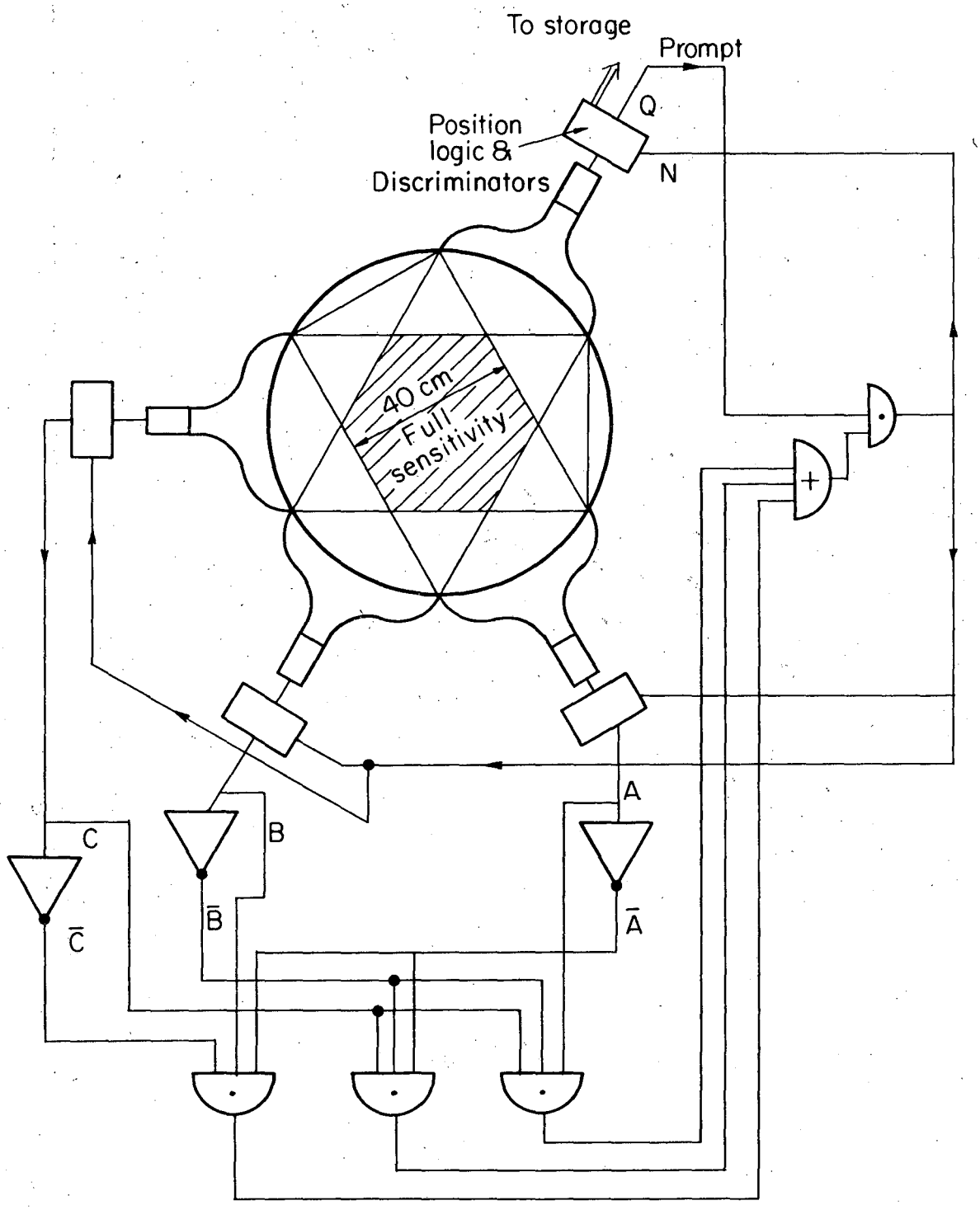

XBL749-4198

Fig. 9

For a collimator opening S (S = 1, 2 or 3 cm) the crystals can receive radiation from a region considerably larger than S (depending on the dimensions of the collimator). On the other hand, valid colinear coincidences can arise only from a region of thickness ~ S/2. The activity external to the section (thickness S) is a major cause of undesired background (see section 5.7) motivating us to extend the collimator as close as possible to the patient.

The collimator is assumed to be about 6 cm thick (10 attenuation lengths). As shown in section 5.7 the overall leakage is 10^{-4} or 5 counts/sec/(μCi per axial cm) which is a small fraction of the total.

4.2 Choice of NaI(Tl) Crystals. A "standard" crystal manufactured by Harshaw Corp. for the Baird-Atomic γ-camera measures 9.5 mm × 9.5 mm × 38 mm long (Fig. 5). To increase the sensitivity and to offer the option of varying the slice thickness, a 8 mm × 30 mm × 50 mm crystal appears more desirable.

4.3 Crystal Position Coding. The detector ring is divided into eight segments of 36 crystals. A position code is created by coupling each crystal to a unique pair of PMTs (Fig. 8). This allows a large number of crystals to be read out by a small number of PMTs (Alvarez, 1960). Moreover, it is possible to reject events where a significant amount of energy has been deposited in more than one crystal of a segment, since in such cases more than two PMTs will respond. This can occur when a gamma ray scatters in the crystals or when two gamma rays are detected in the same segment within the coincidence resolving time.

In general, the maximum number of distinct combinations is given by

$$\frac{n!}{m!\ (n-m)!}$$

where n is the number of PMTs serving each segment and m is the number of PMTs to which each crystal is coupled. In the example of Fig. 8 the code for a segment containing 6 crystals used $n = 4$ and $m = 2$.

The number of PMTs is minimized when $m \approx n/2$, while the number of lightpipes is minimized when m is small. The use of binary and Gray codes will reduce the number of PMTs somewhat further, but will not permit the rejection of multiple detections. The fast digital coding of crystal positions allows each segment to be placed in coincidence with several opposing segments at high rates using a small number of coincidence circuits. Then crystal address codes can be compared to place each crystal in coincidence with a predetermined number of opposing crystals.

For 8 segments of 36 crystals each, the choice of $n = 9$ and $m = 2$ allows 72 PMTs to serve 288 crystals via 576 lightpipes and 12 coincidence circuits.

4.4 Energy and Time Resolution. The energy resolution of a scintillation detector depends on the amount of scintillation light produced, the light collection efficiency, and the quantum efficiency of the PMT at the relevant wavelengths. A 5 cm diam × 5 cm NaI(Tl) crystal can achieve an energy resolution of 8% FWHM for 511 keV gamma rays, but any reduction in the light reaching the PMT (such as by the use of narrow crystals or by coupling the crystal to the PMT via a long lightpipe) will degrade the resolution.

Grenier et al. report an energy resolution of 23% FWHM at 122 keV and 10% FWHM at 662 keV for a 9 × 9 × 38 mm NaI(Tl) crystal coupled directly to a PMT; and a resolution of 50% FWHM at 122 keV when the same crystal was coupled to the PMT via a 61 cm long plastic lightpipe that transmitted 20% of the light. Their data show that, as expected, the width of the photopeak is inversely proportional to the square root of the number of photons reaching the PMT. As the crystals listed in the example of Table 2 are similar in size and would be coupled to the PMTs via similar lightpipes, we can thus expect that at 511 keV the energy resolution will be approximately 50% FWHM × $(122\ \text{keV}/511\ \text{keV})^{\frac{1}{2}}$ = 24% FWHM. Any non-uniformity among the lightpipes will result in a further degradation of the resolution.

The time resolution in NaI(Tl) depends on the same statistical fluctuations that determine the energy resolution. Braunsfurth et al. report a time jitter distribution with a FWHM of 1.3 nsec for 511 keV gamma ray pairs in NaI(Tl), using a system with a good light collection efficiency. We expect that the time jitter distribution of a ring detector system with an energy resolution of 24% FWHM will have a FWHM of 1.3 nsec × (24%/8%) = 3.9 nsec. A 20 nsec coincidence resolving time is assumed in Tables 2 and 3.

4.5 Readout. The readout circuits must perform the following:

1) Determine which PMTs have pulses and convert this information into the binary address of the gamma ray interaction point.
2) Reject events where more than two PMTs in a segment have pulses (i.e., where more than one crystal has received a significant amount of energy). For increased sensitivity at the expense of spatial resolution, it may be desirable to include events where three PMTs have pulses (i.e., where two neighboring crystals have received significant energy). This requires that the code be chosen so that all neighboring crystal pairs generate a unique 3-PMT code.
3) Determine whenever two crystal segments have detected gamma rays within a 10 to 20 nsec time interval.
4) Add the PMT outputs for each coincident crystal segment and reject the event if the pulse height does not fall within a preselected window.
5) Reject the event if another gamma ray is detected (in either coincident crystal segment) within the 200 to 800 nsec required to determine the pulse height.
6) Handle gross counting rates of 2×10^5 sec^{-1} per crystal segment.
7) Collect fan-beam-γ-ray transmission data for the attenuation correction. Figure 7 shows the block diagram of a circuit that meets many of the above requirements.

4.6 Attenuation Corrections. Corrections for attenuation are needed to obtain good transaxial reconstructions. One possibility is the use of a continuous source of positron emitter around the outside of the patient, as suggested by Phelps et al. (1975). Since the attenuation depends only on the line of flight of the two gamma rays and not on the position of the point of annihilation, the attenuation correction for each pair of coincident detectors is the ratio of the transmitted flux before and after the patient is positioned in the system.

A second possibility is the use of a fan beam source of 7.9-yr ^{133}Ba (principal gamma energy 356 keV) that travels 180 degrees around the patient while the opposing 62 crystals collect transmission data. As the attenuation cross section is greater at 356 keV than at 511 keV by a factor of 1.16 for water, muscle and bone (Hubbell, 1969), the attenuation correction for 511-keV pairs is determined as the 0.86 power of the ratio of the transmitted flux of 356 keV gamma rays before and after the patient is positioned in the system. It is necessary to know the attenuation to an accuracy of only 10% rather than the 1% accuracy of the EMI scanner, and approximately 100 times fewer counts are needed. Thus the dose is reduced from 1-3 rad to 50-150 mrad. This second method permits greater ease of source collimation to reduce patient exposure, greater data rates, and the use of an isotope of long half life.

5. PROPERTIES OF THE SYSTEM FOR THE DETECTION OF COINCIDENT ANNIHILATION RADIATION

5.1 Crystal Detection Efficiency. A large slab of NaI(Tl) 5 cm thick detects 511 keV gamma rays with a gross detection efficiency of 82% and a photofraction of 0.79 (Anger, 1966). We have measured the pulse height spectrum for the smaller 0.8 cm × 3 cm × 5 cm deep crystals described here and find that the gross detection efficiency is also 80%, but the photofraction has a lower value of 0.25 due to the loss of Compton scattered gamma rays from the sides of the crystals. In Table 3 we have used a detection efficiency of 50% (100 keV threshold and single crystal interactions only) and a photopeak efficiency of 20%.

5.2 Axial Response Function. Since the two annihilation gamma rays are emitted in nearly opposite directions, true coincident events can only arise from a disc-shaped region of space (called a "section") within the detector circle. The thickness of the section is effectively equal to one-half the corresponding dimensions of the shielding.

A schematic of the detector circle and the collimator circle used to block emissions from outside the section may be seen in Fig. 10. The variable Z is the coordinate along the axis of the detector ring. (Z = 0 at the midplane.) The variable R indicates the distance to that axis.

The sensitivity is maximal at the median place of the section ($Z = 0$) and falls to zero at $Z = \pm S/2$ (the top and bottom surfaces of the section). The dependence of the sensitivity along an axis parallel to the Z axis is called the Axial response Function.

Consider a point at a distance R from the central axis of the detector circle. Consider also two detectors located on opposite sides of the point so that the line between them forms an angle $\emptyset$ with a line connecting the point with $R = 0$ (Fig. 10). Let B_1 be the distance to the closer detector and B_2 be the distance to the farther detector

$$B_1 = \sqrt{C^2 - R^2\sin^2\emptyset} - R\cos\emptyset$$

$$B_2 = \sqrt{C^2 - R^2\sin^2\emptyset} + R\cos\emptyset \qquad (1)$$

The sensitivity is uniform in the central interval $-Z_1 < Z < Z_1$ and falls to zero linearly in the intervals $-\frac{S}{2} < Z < -Z_1$ and $Z_1 < Z < \frac{S}{2}$ (Fig. 11), where

$$Z_1 = \left(\frac{S}{2}\right)\left(\frac{B_2 - B_1}{B_2 + B_1}\right) \qquad (2)$$

Writing the coincident detection probability at Z, R, $\emptyset$ as $f(Z, R, \emptyset)$, we have

$$f(Z,R,\emptyset) = \left(\frac{S+2Z}{S-2Z_1}\right)\left(\frac{\epsilon^2 S}{2B_2}\right) \quad -\frac{S}{2} < Z < -Z_1$$

$$= \frac{\epsilon^2 S}{2B_2} \quad -Z_1 < Z < Z_1$$

$$= \left(\frac{S-2Z}{S-2Z_1}\right)\left(\frac{\epsilon^2 S}{2B_2}\right) \quad Z_1 < Z < S/2$$

$$= 0 \quad Z < -\frac{S}{Z} \text{ or } Z > S/2 \qquad (3)$$

where ϵ is the detector efficiency.

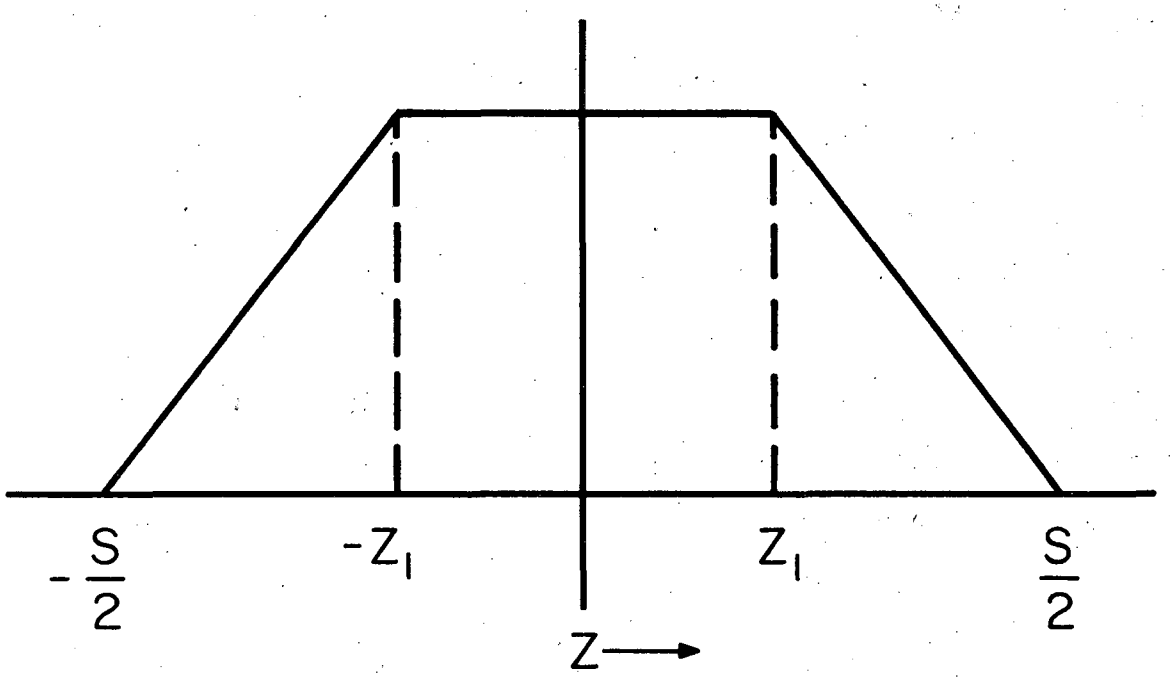

XBL 749-4223

Fig. 11

The axial response function normalized to $f(0,R,\emptyset)$ and averaged over $\emptyset$ is given by:

$$F_A(Z,R) = \int_0^{2\pi} \frac{f(Z,R,\emptyset)}{f(0,R,\emptyset)2\pi} \, d\emptyset \tag{4}$$

This quantity is plotted in Fig. 12 for the case C = 40 cm, S = 2 cm for R = 0 cm, 10 cm and 20 cm.

5.3 Sensitivity. The event rate for the simultaneous detection of two annihilation gamma rays may be calculated as the following product: [contributing activity] × [probability of photon #1 reaching a detector] × [probability of photon #2 reaching a detector] × [product of detector efficiencies]. This formulation is used below for both unscattered gamma rays (Eq. 5) and scattered gamma rays (Eqs. 15 & 18).

The unscattered coincident event rate C_o of a ring detector is approximated by:

$$C_o = \left[\frac{\rho a S}{2}\right] \left[\frac{S\ e^{-\mu L}}{2c}\right] [\varepsilon^2] = \left[\frac{\rho a S^2\ e^{-\mu L}\ \varepsilon^2}{4c}\right] \tag{5}$$

where

ρ = activity density in μCi per axial cm

a = 37,000 annihilations per sec per μCi of β^+ (conversion factor)

S = exposed dimension of detector ring along ring axis (determined by width of shielding slit) (see Fig. 10)

$e^{-\mu L}$ = probability that neither gamma ray scatters in the tissue

μ = narrow beam attenuation coefficient for 511-keV gamma rays in tissue (in water $\mu = 0.10\ cm^{-1}$)

L = tissue thickness

c = radius of detector ring

ε = detection efficiency for 511-keV gamma rays.

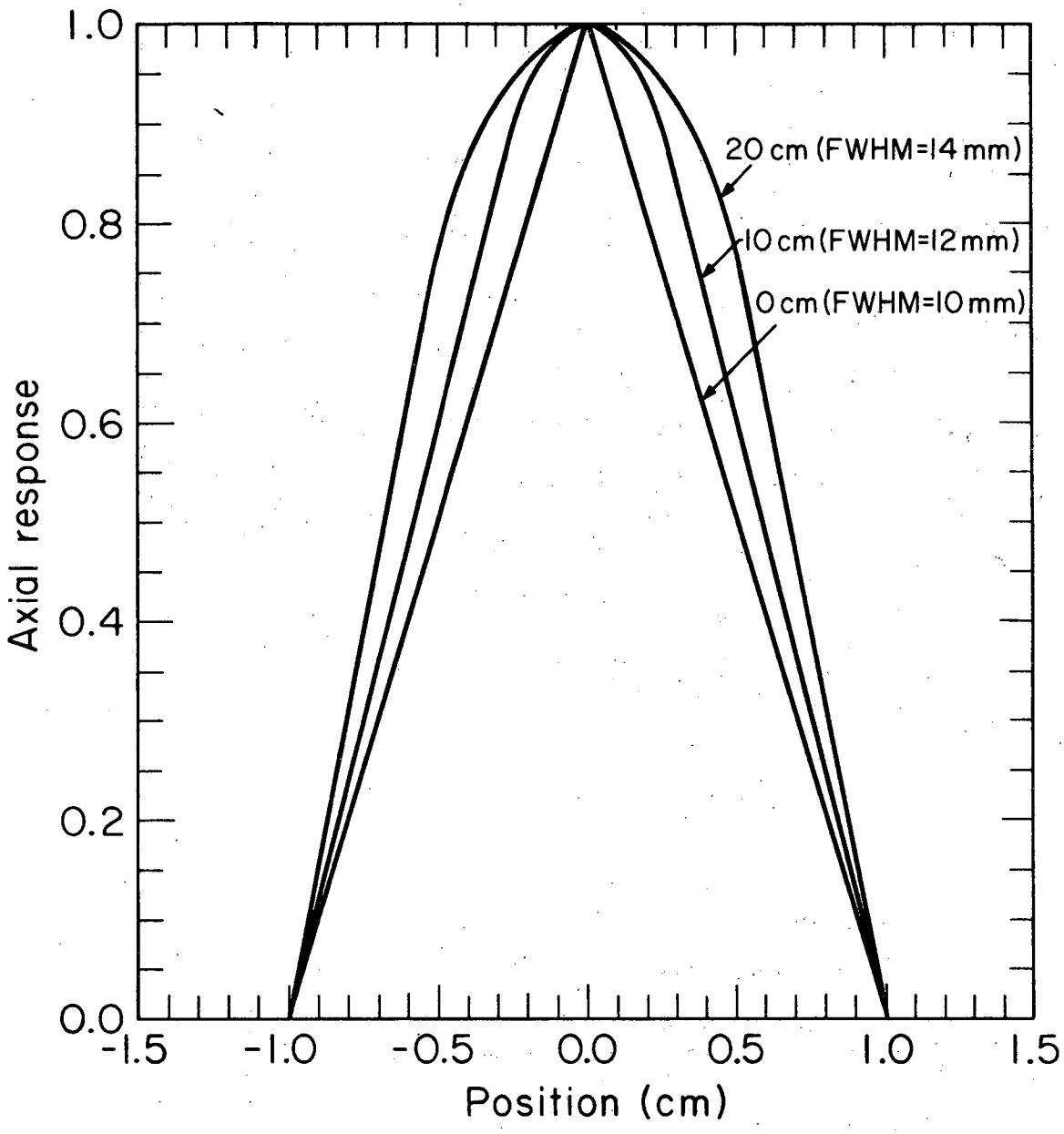

XBL749-4227

Fig. 12

The first bracket is the contributing activity; the second bracket is the probability that both gamma rays reach the detector ring without having scattered; and the third bracket is the probability that both gamma rays are detected and pass the pulse height threshold.

For the case 1 of Table 3, C = 40 cm, S = 2 cm, E = 50%, $\mu L = 2$ (20 cm diam cylinder of tissue) the sensitivity is:

$$C_o = \left(\frac{37{,}000 \times 2}{2}\right)\left(\frac{2e^{-2}}{2 \times 40}\right)(0.50)^2 \qquad (6)$$

$$= 31 \text{ events/sec/[}\mu\text{Ci of } \beta^+ \text{ per axial cm]}$$

We assume that the source distribution lies within a distance R from the ring axis given by:

$$R = c \sin (f\pi/2) \qquad (7)$$

where each detector (of a total of N) is in coincidence with the fN opposing detectors. For a circular ring the geometrical sensitivity is nearly uniform within the radius R. We also assume that the detectors are densely packed around the ring and that the shielding blocks only gamma rays external to the section being imaged.

In Table 3 we have calculated the sensitivity C_o/ρ and many other parameters for a particular positron ring detector system and a tissue thickness of 20 cm ($\mu L = 2$). In Case I the event rate is 6000 events per sec for $\rho = 200$ μCi per axial cm. Thus if the section is to be resolved into a grid of 40 X 40 pictels, 375 events can be collected per pictel over a 100-sec time period.

The greater imaging sensitivity of the positron ring detector over conventional single gamma imaging arises primarily from a greater solid angle. The ring detector has a solid angle factor of S/2c which is 2.5×10^{-2} for the example of Table 3. In single gamma imaging only a small area of the crystal ($\sim \pi d^2/4$ for a resolution distance d) receives gamma rays from sources at a typical imaging distance D. For low photon energy, the resulting solid angle factor is approximately $(\pi d^2/4)/(4\pi D^2) = 5.6 \times 10^{-5}$ for d = 6 mm and D = 20 cm. Thus in these examples the positron ring detector has approximately 450 times greater solid angle than single gamma imaging with the additional benefit of transaxial tomography without rotation.

5.4 Effect of the Range of Positrons in Tissue. The line spread function for positrons in water has been measured for a variety of isotopes (Cho et al., 1975). For the worst case (^{82}Rb, 3 MeV beta end point), the range of the positrons introduces an rms of about 1.5 mm.

5.5 Effect of Deviations from 180° Line of Flight. In most solids and liquids, annihilation occurs before the positron has fully thermalized. Typical energies are 10 to 20 eV and result in angular distributions about 180° with FWHM of 6-9 mr. Specific examples include water at +4°C (FWHM = 8.5 mr, FW0.1M = 18 mr) (Colombino et al., 1965) and calcium metal (FWHM 6.5 mr, FW0.1M = 13 mr) (Stewart 1957). For the positron ring system described here (crystal radius 40 cm) an angular uncertainty with FWHM of 8 mr corresponds to a position uncertainty with FWHM 1.6 mm.

5.6 Transaxial Resolution Function. Each point within the section will be viewed by many pairs of detectors and for points not on the central axis of the detector circle, each pair will have a different resolution. This difference is due to the fact that the effective size of a detector depends on the viewing angle. Detector pairs disposed along a diameter (such as III and IV in Fig. 13) view point p with better resolution than those disposed along a chord (such as I and II in Fig. 13).

Let us assume that each detector has a length L (in the R direction), a height H (in the Z direction) and a width W. The detector circle radius is C. For a parallel group of rays having an angle θ with respect to the length of the detector (Fig. 14), the path length $D(x,\theta)$ through the detector is given by the following equations:

For $\theta < \theta_c$

$$
\begin{aligned}
D(x,\theta) &= 0 && \text{for } x < 0 \text{ or } x > x_{max} \\
D(x,\theta) &= \frac{x}{\sin\theta\cos\theta} && \text{for } 0 < x < L\sin\theta \\
D(x,\theta) &= \frac{L}{\cos\theta} && \text{for } L\sin\theta < x < W\cos \\
D(x,\theta) &= \frac{x_{max} - x}{\sin\theta\cos\theta} && \text{for } W\cos\theta < x < x_{max}
\end{aligned}
\qquad (8)
$$

where $x_{max} = L\sin\theta + d\cos\theta$

and $\theta_c = W/L$

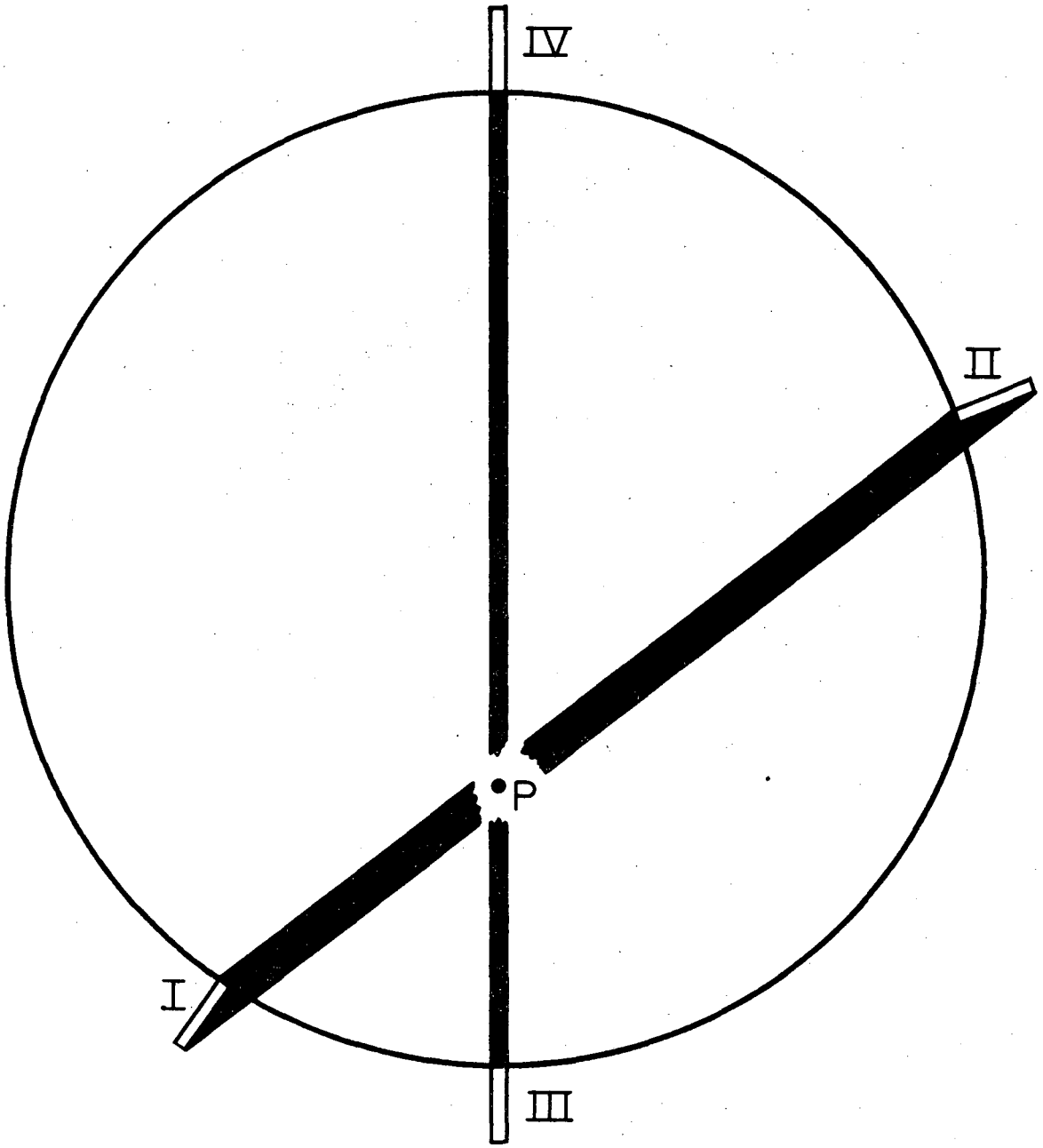

XBL 749-4224

Fig. 13

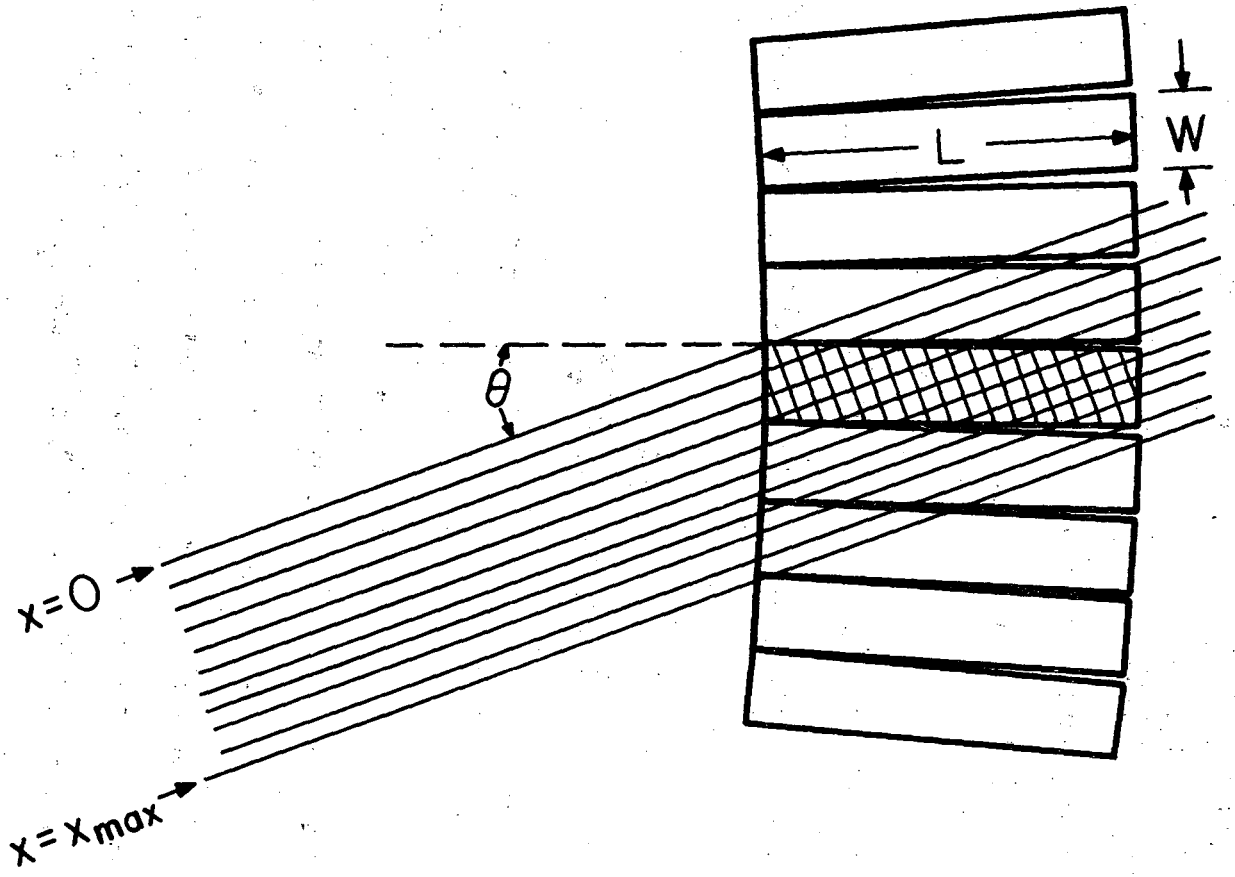

XBL749-4225

Fig. 14

For $\theta > \theta_c$

$$D(x,\theta) = 0 \qquad \text{for } x < 0 \text{ or } x > x_{max}$$

$$D(x,\theta) = \frac{x}{\sin\theta\cos\theta} \qquad \text{for } 0 < x < W\cos\theta \tag{9}$$

$$D(x,\theta) = \frac{W}{\sin\theta} \qquad \text{for } W\cos\theta < x < L\sin$$

$$D(x,\theta) = \frac{x_{max} - x}{\cos\theta\sin\theta} \qquad \text{for } L\sin\theta < x < x_{max}$$

The absorption path $A(x,\theta)$ due to passage through other detectors is given by the following equations:

$$A(x,\theta) = 0 \qquad \text{for } x < W\cos$$

$$A(x,\theta) = \frac{x - W\cos\theta}{\cos\theta\sin\theta} \qquad \text{for } W\cos\theta < x < x_{max} \tag{10}$$

We write the photopeak detection probability for a gamma ray at angle θ as

$$P(x,\theta) = \left[\mathrm{EXP}\left(-A(x,\theta)\mu_A\right)\right] \left[1 - \mathrm{EXP}\left(-D(x,\theta)\mu_D\right)\right] \tag{11}$$

where μ_A is the coefficient for absorbing more than 511 keV - E_p, μ_D is the coefficient for absorbing more than E_p, and E_p is the effective pulse height threshold for each crystal. The first bracket is the probability that a 511 gamma ray will emerge from a thickness $A(x,\theta)$ of NaI and retain an energy greater than E_p, while the second bracket is the probability that a 511 gamma ray will deposit more than E_p on passing through a thickness $D(x,\theta)$ of NaI. For a threshold E_p = 410 keV, we estimate $\mu_A = 0.25\ \mathrm{cm}^{-1}$ and $\mu_D = 0.12\ \mathrm{cm}^{-1}$.

The line spread function g(R,x) at a distance R from the ring axis is given by

$$g(R,x) = \int_0^{2\pi} \frac{d\phi}{2\pi} \int_{-\infty}^{\infty} dx' \, P(x + x', \theta) \, P(x - x'', \theta) \left(\frac{S^2/2}{B_1 + B_2} \right) \qquad (12)$$

where $\sin\theta = \frac{R}{c} \sin\phi$, and $x'' = x' \, B_2/B_1$.

It is assumed that in the interval $0 < x' < x_{max}$, θ is essentially constant. This is true whenever $W \ll B_1$.

The function g (R,x) is plotted in Fig. 15 for R = 0 cm, 10 cm, and 20 cm under the assumptions: W = 0.8 cm, L = 3.8 cm, C = 40 cm, $\mu_A = 0.25\ cm^{-1}$, $\mu_D = 0.12\ cm^{-1}$. Although the detection probability $P(x,\theta)$ is not a symmetric function in x, we see that g(R,x) is quite symmetric about x = 0. The FWHM of g(R,x) is plotted in Fig. 16 as a function of R.

5.7 Shielding and Backgrounds. Shielding is essential for blocking gamma rays emitted by activity external to the section being imaged. Furthermore, varying the width of the shielding slit allows the section thickness to be varied. True unscattered coincident events can arise only from a positron activity $\frac{\rho S}{2}$ within the section, but scattered coincident events and single counts (both of which contribute to the background) can arise from an activity that is effectively $\frac{\rho c S}{T}$, where T is the depth of the shielding slit (Figs. 10, 17, 18).

There are two additional methods available for rejecting scattered gamma rays. The coincidence requirement (i.e., that each of the N detectors be in coincidence with the fN opposing detectors) establishes an approximate upper limit $\Theta_f = f\pi$ on the scattering angle. This

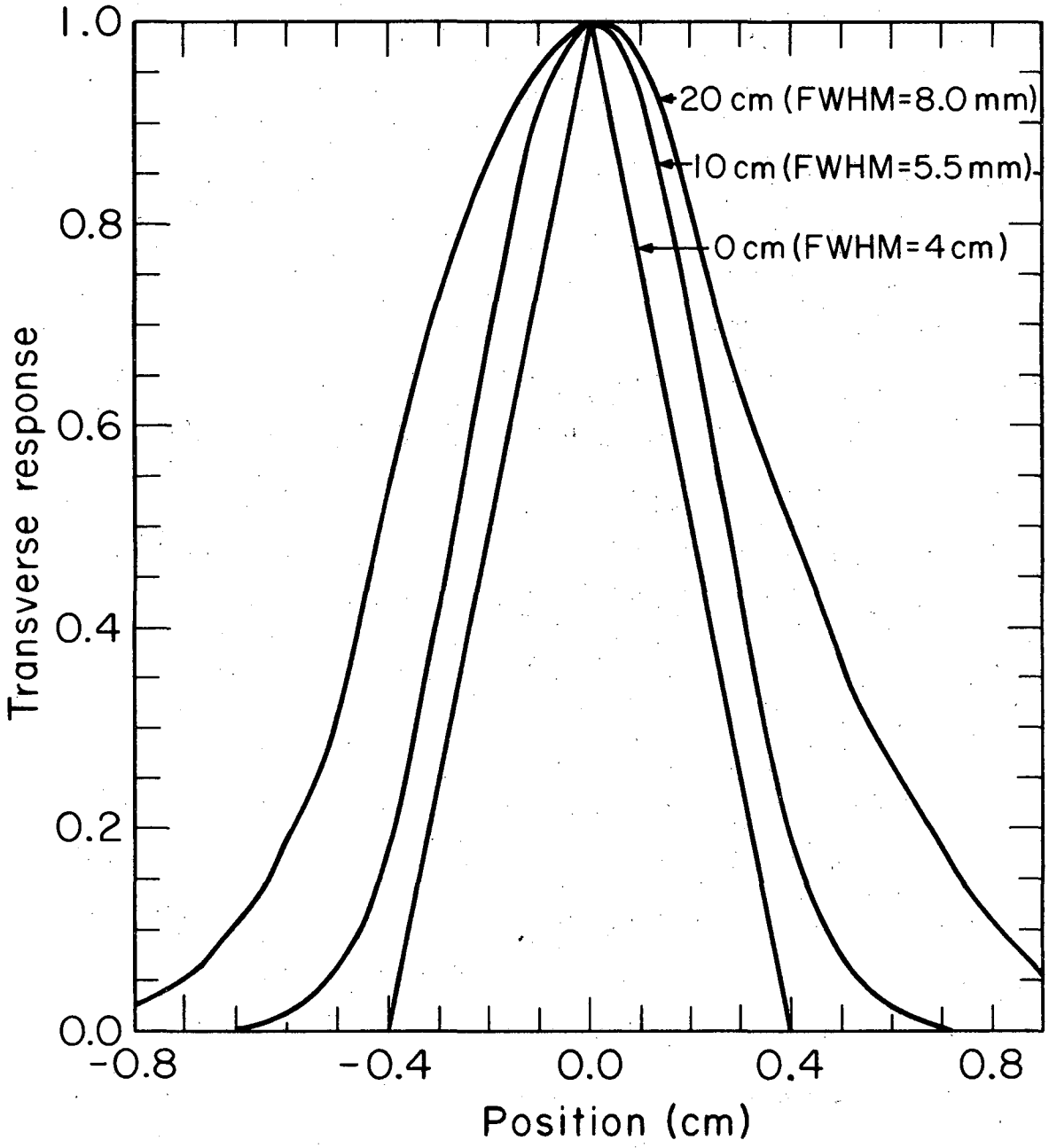

XBL 749-4220

Fig. 15

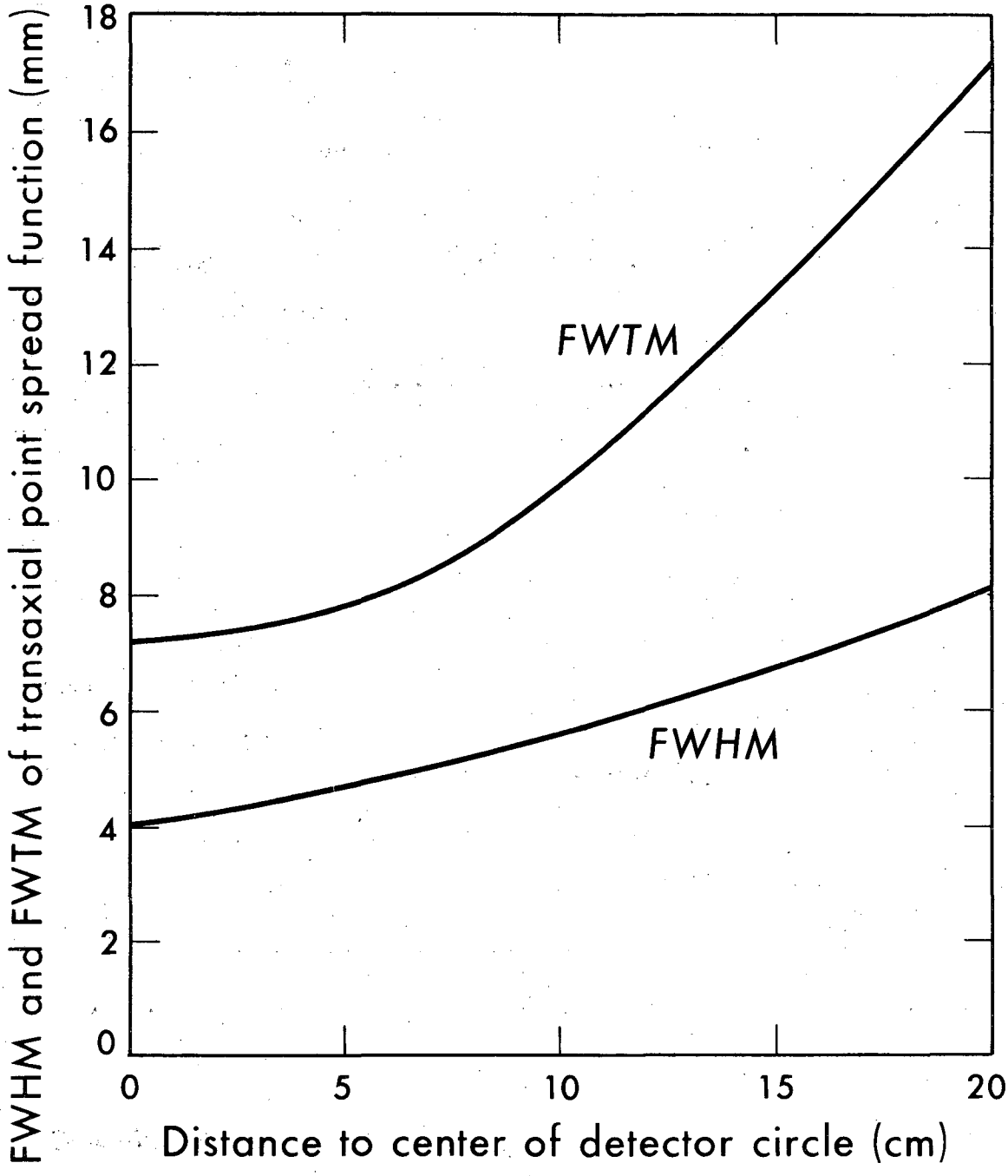

XBL 757-3459

Fig. 16

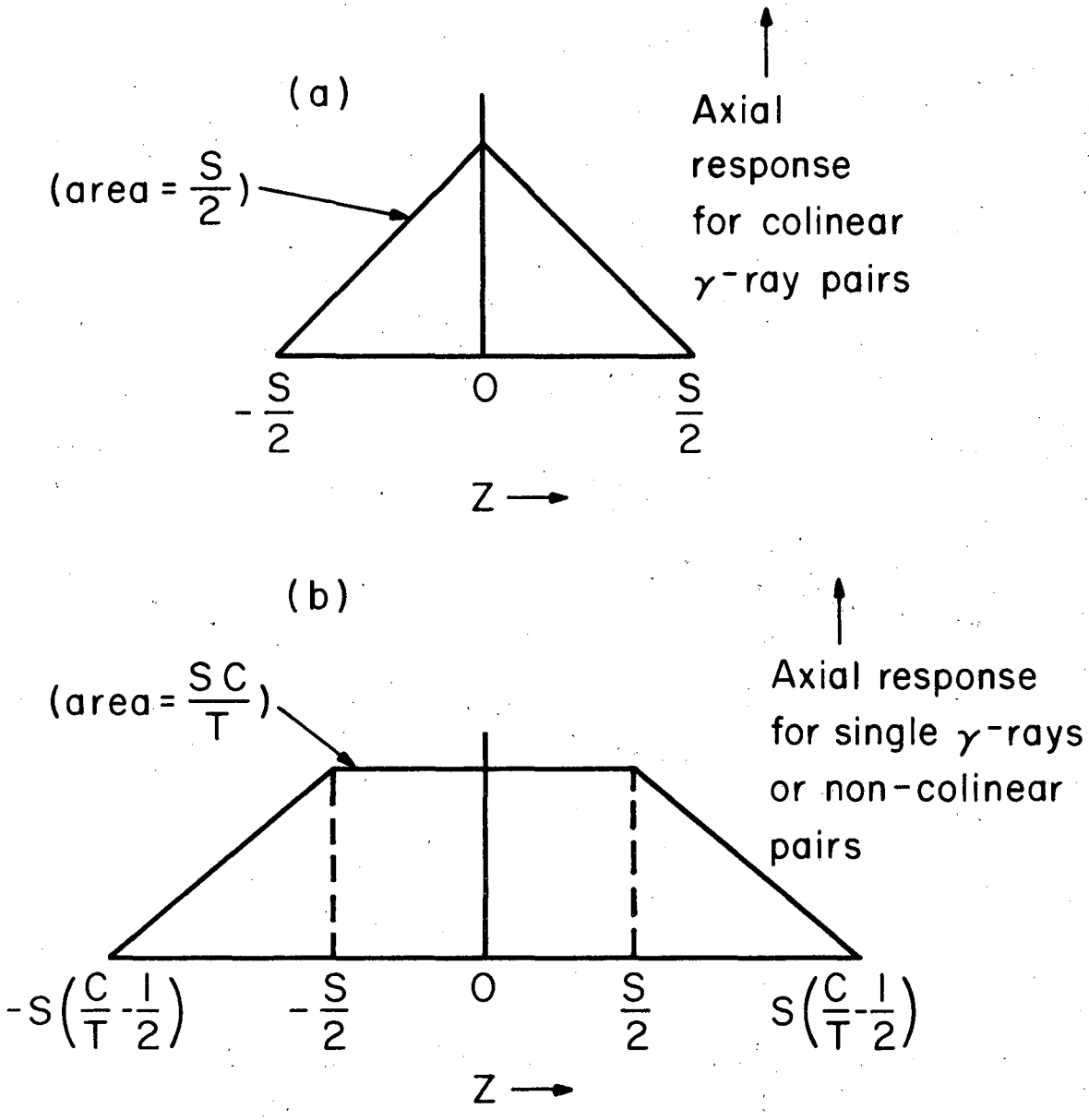

XBL749-4228

Fig. 17

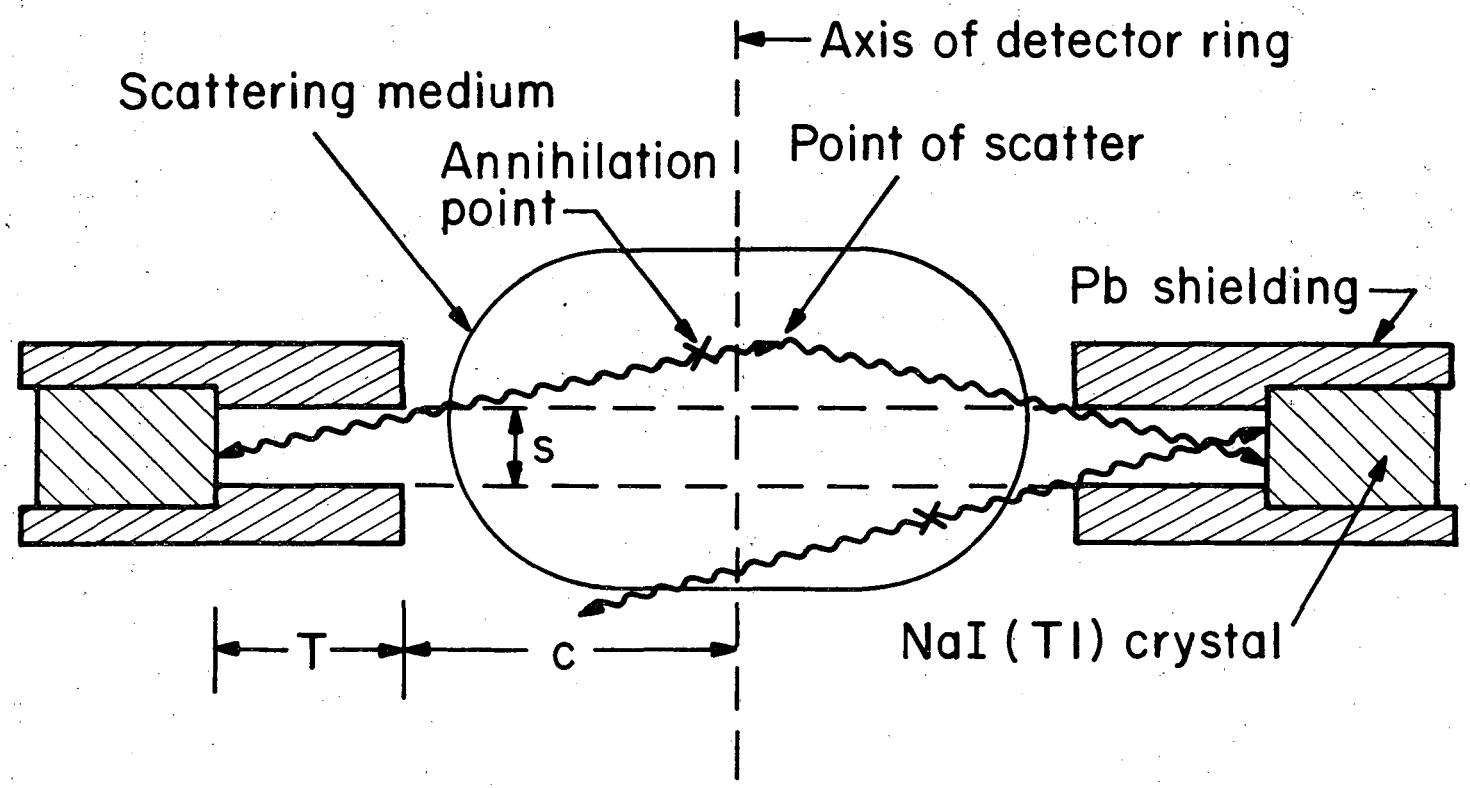
Axis of detector ring
Scattering medium
Annihilation point
Point of scatter
Pb shielding
s
T
c
NaI (Tl) crystal
XBL 753-2535

Fig. 18

approximation is realistic, as the size of the scattering medium is usually small compared to the diameter of the detector ring. The second method is the use of a pulse height threshold that rejects scattered gamma rays with an energy below E_p. In single Compton scattering this corresponds to a maximum scattering angle Θ_p (AIP Handbook, 1972, Eq. 8 e-5):

$$\cos(\Theta_p) = 2 - \frac{511 \text{ keV}}{E_p} \tag{13}$$

For plot, see Fig. 19.

For scattered coincident events the effective maximum scattering angle Θ_m is the smaller of Θ_f and Θ_p. (For single counts the maximum scattering angle is always Θ_p). The effective minimum scattered gamma ray energy E_m corresponding to θ_m is given by:

$$E_m = \frac{511 \text{ keV}}{2 - \cos(\theta_m)} \tag{14}$$

Scattered Coincident Backgrounds. The rate of scattered coincident events where only one member of the annihilation pair scatters is approximated by:

$$C_1 = \left[\frac{\rho a S c}{T}\right] \left[\frac{S(1-P_s')}{c}\right] \left[\frac{P_s g_1 S}{c}\right] [\varepsilon\varepsilon_m] = \frac{\rho a S^3 g_1 \ \varepsilon\varepsilon_m \ P_s(1-P_s)}{T_c} \tag{15}$$

where $P_s = 1 - e^{-\mu L/2}$, the probability a 511 keV gamma ray will scatter on passing through half the tissue,

ε_m is the average detection efficiency for gamma rays between energy E_m and 511 keV, and g_1 is a solid angle factor. The first bracket is the contributing activity; the second bracket is the probability that either gamma ray reaches a detector without scattering;

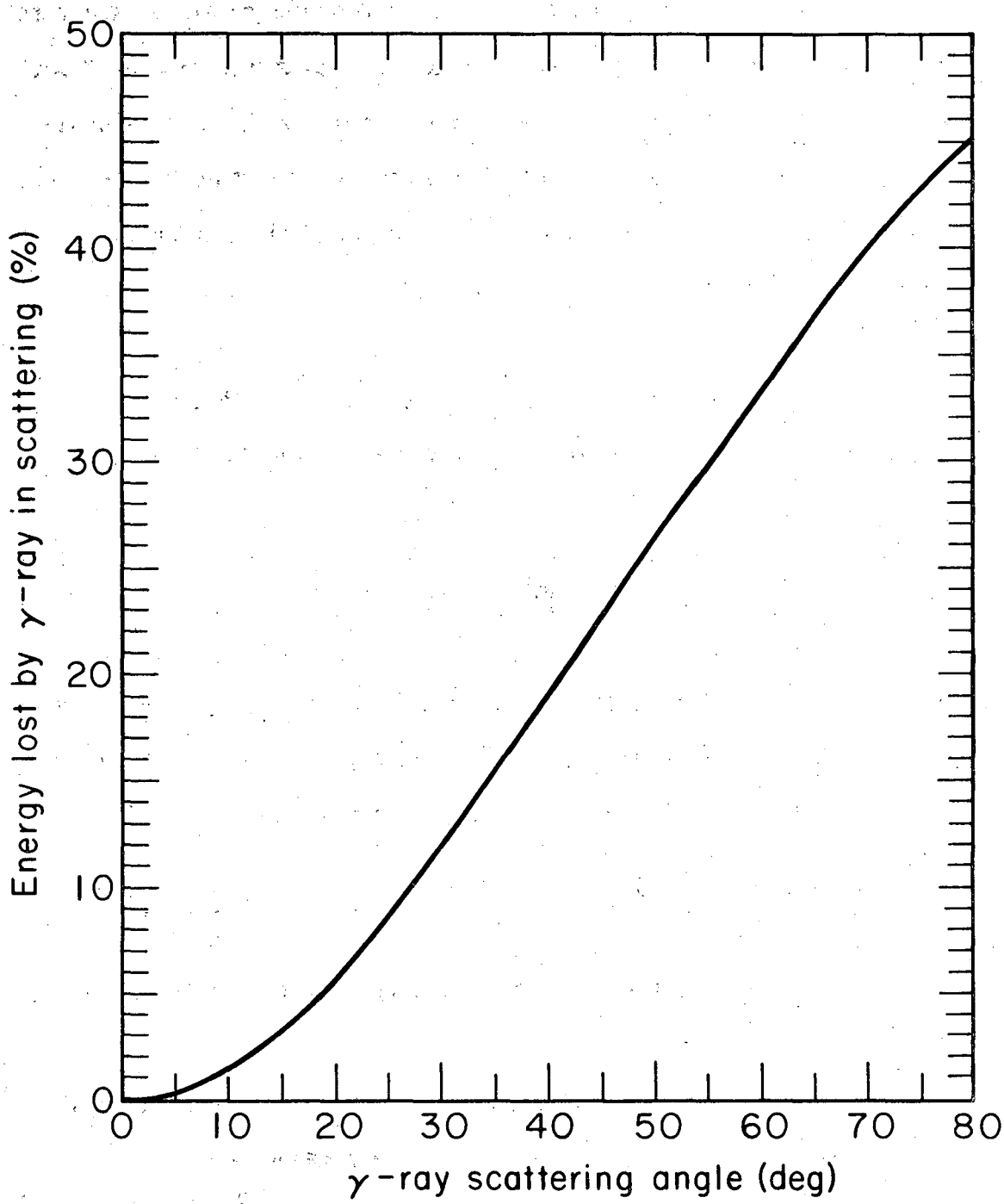

XBL749-4221

Fig. 19

the third bracket is the probability that the other gamma ray scatters and reaches one of the opposing (coincident) detectors; and the fourth bracket is the probability that both gamma rays are detected and pass the pulse height threshold. This expression assumes that the activity is near the center of the scattering medium, that the scattering takes place close to the axis of the ring, and that single scattering predominates.

The dimensionless quantity g_1 describes the fraction of Compton scattering angles that fall within the angular strip S/c wide and $2\theta_m$ long:

$$g_1 = \frac{\int_{-\theta_m}^{\theta_m} \frac{d\sigma}{d\Omega}\, d\theta}{\int_0^{\pi} 2\pi \frac{d\sigma}{d\pi} \sin\theta \, d\theta} \qquad (16)$$

where $\frac{d\sigma}{d\Omega}$ is the differential cross section for Compton scattering of 511 keV gamma rays on free electrons, given by the Klein-Nishina formula (AIP Handbook, 1972, Eq. 8e-13) (for plot see Fig. 20):

$$\frac{d\sigma}{d\Omega} = 11.91 \times 10^{-26}\ \mathrm{cm}^2/\mathrm{str/electron}\ \frac{(1 - \cos\theta + \cos^2\theta - \frac{1}{3}\cos^3\theta)}{(2 - \cos\theta)^3} \qquad (17)$$

and θ is the γ-ray scattering angle. See Table 4 for values of g_1 as a function of θ_m.

The rate of scattered coincident events C_2 where both members of the annihilation pair have scattered is approximated by:

$$C_2 = \left[\frac{\rho a S c}{T}\right] \left[\frac{S P_s}{2c}\right] \left[\frac{P_s g_2 S}{c}\right] [\varepsilon_m^2] = \frac{\rho a\ S^3 g_2\ \varepsilon_m^2\ P_s^2}{2Tc} \quad . \qquad (18)$$

The first bracket is the contributing activity, the second bracket is the probability that one gamma ray scatters and reaches the detectors;

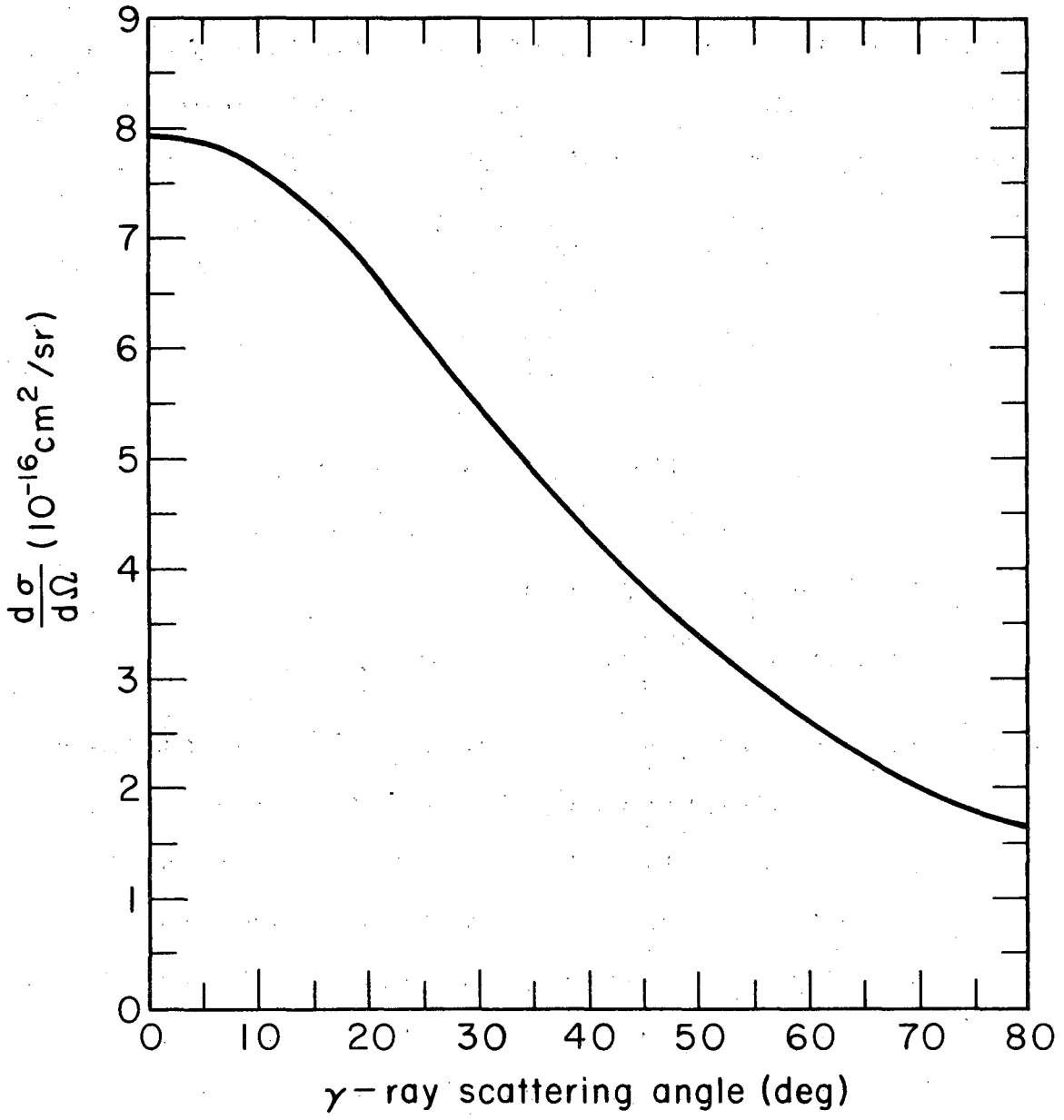

XBL749-4222

Fig. 20

the third bracket is the probability that the other member of the pair also scatters and reaches one of the opposing (coincident) detectors; and the fourth bracket is the probability that both gamma rays are detected and pass the pulse height threshold. Assuming that single scattering predominates for each gamma ray, g_2 is given by

$$g_2 = \frac{\int_{-\theta_m}^{\theta_m} \frac{d\sigma^*}{d\Omega}\, d\theta}{\int_0^{\pi} 2\pi \frac{d\sigma^*}{d\Omega} \sin\theta\, d\theta} \tag{19}$$

where $\frac{d\sigma^*}{d\Omega}$ is the autocorrelation of $\frac{d\sigma}{d\Omega}$. See Table 4 for approximate values of g_2 as a function of θ_m. The total background rate C_b from scattered coincident events is given by:

$$C_b = C_1 + C_2 = \frac{\rho a S^3}{2T_c}\left[2g_1\, \varepsilon\varepsilon_m P_s(1-P_s) + g_2\, \varepsilon_m^2 P_s^2\right] . \tag{20}$$

Note that the backgrounds C_1 and C_2 are not associated with time resolution but with scatter geometry and energy resolution. As expected, the ratio of scattered coincident events C_b to unscattered coincident events C_o is lowest for "good scatter geometry" (i.e., small S/T).

Associated Gamma Rays. Many important positron emitting isotopes (such as ^{82}Rb and ^{68}Ga) have accompanying gamma rays that are emitted essentially in time coincidence with the 511 keV gamma ray pair. The rate of background events C_γ where an annihilation gamma ray is detected in coincidence with an accompanying gamma ray is approximated by:

$$C_\gamma = \left[\frac{2\rho a S c}{T}\right]\left[\frac{f s^2}{4c^2}\right] [F_\gamma \in_\gamma \in] \tag{21}$$

where F_γ is the probability of emission of the accompanying gamma ray

and $\in_\gamma$ is its detection efficiency. This expression is an overestimate in that it includes all detected gamma rays, whether they have scattered in tissue or not (i.e., it does not consider that scattered gamma rays have a reduced chance of producing pulses in the pulse height window). The first bracket is the rate of emission of 511 keV gamma rays, the second bracket is the probability that a 511 keV gamma ray reaches the detector ring while an accompanying gamma ray reaches one of the opposing (coincident) detectors, and the third bracket is the probability that the accompanying gamma ray is emitted and both gamma rays are detected. For the example of Table 2 and ^{82}Rb,

$$C_\gamma = \left(\frac{2\times200\times37{,}000\times2\times20}{20}\right)\left(\frac{.22\times2^2}{4\times40^2}\right)(0.1\times0.3\times0.43) = 53 \text{ counts/sec} \quad (22)$$

<u>Single detection backgrounds</u>. The single counting rate C_2 is given by:

$$C_s = \left[\frac{2\rho aSc}{T}\right]\left[\frac{S}{2c}\right]\left[\varepsilon(1-P_s) + \varepsilon_p P_p\right] = \frac{\rho aS^2}{T}\left[\varepsilon(1-P_s) + \varepsilon_p P_p\right] \quad (23)$$

where P_p is the probability that a gamma ray will scatter in tissue and retain an energy greater than E_p (i.e., the pulse height threshold) and ε_p is the average detection efficiency for such gamma rays. The first bracket is the contributing activity; the second bracket is the solid angle factor of the detector ring; and the third bracket is the sum of the probability for not scattering and being detected and the probability for scattering and being detected. For the single Compton scattering of 511-keV gamma rays,

$$P_p \approx P_s\left[\frac{5/2 + 3\,\ell n\alpha + 1/\alpha - 3\alpha - \alpha^2/2}{40/9 - 3\,\ell n3}\right] \quad (24)$$

where $\alpha = E_p/511$ keV and $1/3 \leqslant \alpha \leqslant 1$. The quantity in brackets is the

probability that the scattered photon will have an energy greater than E_p, derived by integrating Eq. 8e-21 of Gray, The AIP Handbook, 1972.

Accompanying gamma rays can also contribute a background counting rate $C_{S\gamma}$:

$$C_{S\gamma} = \left[\frac{\rho a S c}{T}\right]\left[\frac{S}{2c}\right][F_\gamma E_\gamma] \tag{25}$$

This expression includes all detected accompanying gammas, whether they have scattered in tissue or not. For the example of ^{82}Rb and Table 3,

$$C_{S\gamma} = \left[\frac{200 \times 37{,}000 \times 2 \times 40}{20}\right]\left[\frac{2}{2 \times 20}\right][0.1 \times 0.3] \tag{26}$$

$$= 44{,}400 \text{ counts/sec} .$$

Two other single detection backgrounds are also present, the rate of PMT noise pulses within the pulse height window (negligible and not considered further), and C_L the rate for the process in which a gamma ray penetrates or scatters in the lead shielding, is detected and passes the pulse height threshold. In calculating C_L, we assume that the detectors are shielded by 10 attenuation lengths of lead (6.1 cm) in all directions where appreciable activity is present. The probability of penetration (no interaction in the lead) is $e^{-10} = 4.5 \times 10^{-5}$. To include the gamma rays that scatter in the lead and escape, we use the buildup factor of 2.3 from Goldstein et al. (1954). As shown in the same reference, 75% of the scattered photons escaping 10 attenuation lengths of lead have energies above 400 keV. Thus the overall leakage probability (penetration plus scatter) is $P_L = 1.0 \times 10^{-4}$. We note that the product of the detection efficiency and the solid angle

subtended by the detectors is very nearly the same for points within 30 cm of the midplane. We therefore use the detection efficiency and solid angle associated with the midplane. In this case we also assume that the available activity extends over 60 cm of the central axis.

$$C_L = (2a\rho \times 60)\ (\frac{S}{2C})\ (\in)\ (P_L) \tag{27}$$

In the example of Table 3,

$$C_L = (2 \times 200 \times 37{,}000 \times 60)\ (\frac{2}{2\times 40})\ (.50)\ (1.0 \times 10^{-4}) \tag{28}$$

$$= 1100 \text{ counts/sec} .$$

<u>Accidental Coincidence Background</u>. The accidental coincidence rate C_a is given by:

$$C_a = fC_s^2 t/2 \tag{29}$$

where t is the time resolution. It is of importance to calculate the maximum rate $\hat{C}_o$ for a certain fraction $\eta = C_a/C_o$ of accidental coincidences:

$$\hat{C}_o = \frac{\eta T^2\ \varepsilon^4 (1-P_s)^4}{8\ ftc^2\ [\varepsilon(1-P_s) + \varepsilon_p P_p]^2} \tag{30}$$

As expected, the maximum event rate is enhanced by good time resolution, good shielding, and good detection efficiency. It is important to reduce f to the point where all (or almost all) of the activity lies within the radius R (Eq. 7). Reducing f below this value will reduce the signal C_o approximately as f^2 (without effecting the single counting rate C_s) and actually cause $\hat{C}_o$ to decrease.

For the example of Case I of Table 3 and for a 20% accidental coincidence rate ($\eta = 0.20$), we have

$$\hat{C}_o = 3500 \text{ events per sec}$$

and

$$\rho = 110 \ \mu\text{Ci per axial cm.}$$

The profound effect that the scattering medium has on the maximum event rate can be seen by noting what these values would be in the absence of the scattering medium (i.e., $P_s = P_p = 0$):

$$\hat{C}_o = 350{,}000 \text{ events per sec}$$

and

$$\rho = 1500 \ \mu\text{Ci per axial cm.}$$

One should note that: (a) increasing T (whenever possible) by extending the collimator closer to the patient reduces all backgrounds without reducing the sensitivity; (b) increasing the section thickness S increases the sensitivity as S^2, but the scattered coincident background increases as S^3; (c) the maximum event rate $\hat{C}_o$ (as limited by accidentals) is not a function of S. In Table 3 we have calculated these backgrounds for a particular activity level and for several pulse height windows. While these backgrounds are 30-45% of the total number of events, they are fairly uniform over the entire image and contribute little relative to regional concentrations of activity (e.g., in the myocardium).

5.8 Deadtime. Deadtime arises from the limited speed of both the scintillation process and the electronic circuits. After the interaction of a gamma ray in NaI(Tl), 800 nsec is required to collect 90% of the available scintillation light (91% of the light is emitted with an exponential time constant of 218 nsec and 9% is emitted with an exponential time constant of 1340 nsec) (Tidd et al., 1973). To preserve pulse height information to within 10% at high counting rates, it is necessary to reject all counts that occur within approximately 800 nsec of another count. This requirement results in a paralyzing deadtime of 800 nsec for each coded segment of the ring. The circuits that perform the pulse height selection may also introduce a paralyzing deadtime, but by proper design it is possible to limit the overall paralyzing deadtime t_p to 1 μsec (Blatt et al., 1968). The circuits that handle the time coincidence and position information introduce a non-paralyzing deadtime t_n of $\leqslant$ 200 nsec, but this does not result in an appreciable loss of counts, provided the circuits are properly designed and $t_n \leqslant t_p$.

In Cases II and III of Table 3, where a pulse height selection is imposed, the fraction of time that each 36 crystal segment is available is e^{-Gt_p}, and the fraction of counts f_c lost per segment is given by:

$$f_c = 1 - e^{-Gtp} \quad . \tag{31}$$

G is the gross counting rate for each segment (1.3×10^5), t_p = 1 μsec, and the fraction of counts lost (f_c) is 12%. As a coincident event

requires that two segments be available for counting (probability = e^{-2Gt_p}), the fraction of coincident events f_e lost is given by

$$f_e = 1-e^{-2Gt_p} \tag{32}$$

and equal to 23% for this example.

In Case I of Table 3 no pulse height selection is imposed, and we assume that the paralyzing deadtime can be reduced to 200 nsec. In this case the fraction of counts lost (f_c) is 2.5% and the fraction of events lost (f_e) is only 5%, but the backgrounds are larger (see Table 3).

6. DATA ANALYSIS

6.1 Interface. The procedure involved in the reconstitution of the coincidence events involves interfacing a small digital computer to the output from the imaging device. The data position information is configured in 16-bit digital words to identify which of the 8,928 crystal pairs were in coincidence for the particular event. The data are stored in one of two modes, histogram or list, depending upon the final configuration for the microprocessor which will be used to configure the digital words. A number of schemes have been envisioned. One scheme is to calculate the projection angle and ray position by simply noting the relative angular positions of the coincident detectors θ_1, θ_2 with respect to some reference line. The angle of the projection plane 90° orthogonal to the line of position somewhere on which the event occurred is given by

$$\theta_1 + \frac{\theta_2 - \theta_1}{2} \tag{33}$$

With this projection angle and a knowledge of the position of one of the detectors on the periphery, it is straightforward to calculate the ray $P_{k\theta}$ associated with the event. Data are then histogrammed in terms of equivalent projections by adding for each angle θ the events that belong in similar k's. By this means a projection of data will be reconstituted and appear similar to data which would have been obtained if 144 views were made using a parallel hole collimator.

6.2 Reconstruction Algorithms. Once the data have been accumulated, both transmission and emission, the reconstruction of the transverse section will proceed by one of five techniques:

1. iterative least squares
2. Fourier methods
3. convolution hardwire technique
4. direct hardwire technique
5. Marr's technique.

We have explored various algorithms using emission and transmission (Budinger and Gullberg, 1974a) and are still not satisfied which technique would be optimum for our system. The reason for this is that new devices such as hardwire two-dimensional Fourier transform packages might favor the Fourier two-dimensional technique over the Fourier technique, or the availability of charged coupled computing devices (Tiemann et al., 1974) and read only memory, or microprocessors might lead to the algorithm employing hardwired electronics rather than a digital computer. We have been actively working in this field for a number of years, and see a great potential in a microprocessor approach.

Comparison of some of the techniques is shown as Fig. 21. Figure 22 shows a difference between the result of reconstruction of 36 projections on the letters L O V on a 64 × 64 array using the back projection of filtered projections (convolution) technique and the iterative least squares technique. The Fourier filter technique does not handle noise well but is 80 times faster to implement than the iterative least squares technique. We have explored techniques of applying a Butterworth filter in digital form to the back projection

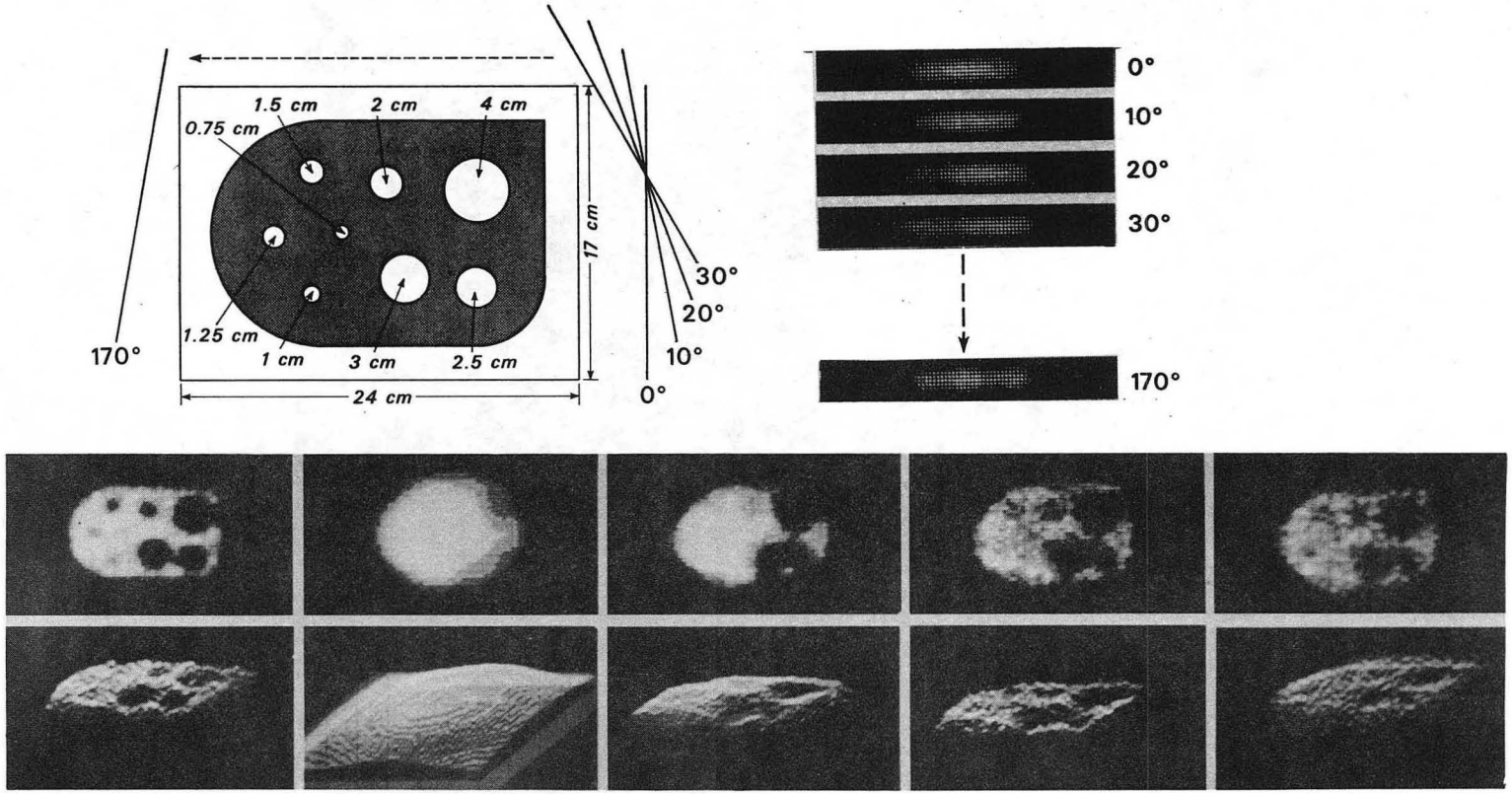

XBB 736-4066

Fig. 21

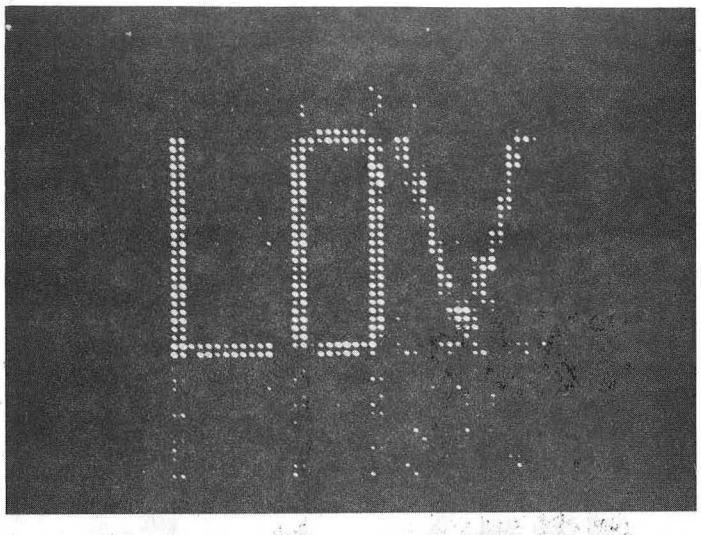

FILTERED BACK PROJECTION

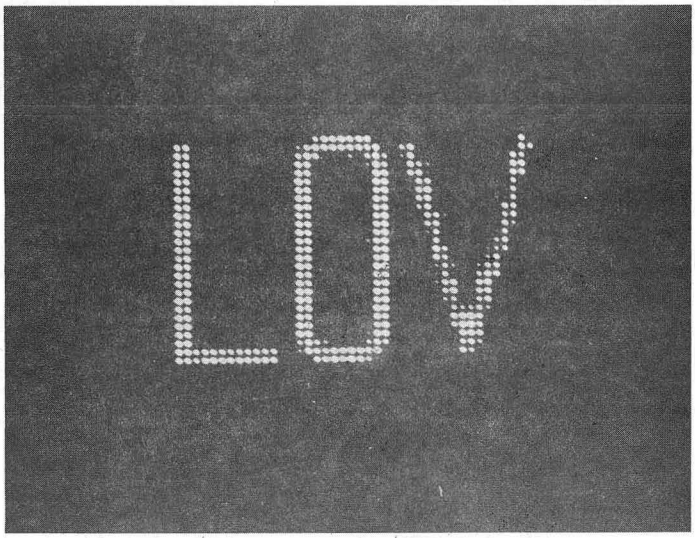

LEAST SQUARES

XBB 749-6014

Fig. 22

of filtered projections technique with some improvement. The noise associated with positron coincidence detection scheme might be of less importance than that which we have experienced with conventional gamma imaging. Thus the filtered back projection technique with roll-off filters we have explored might be adequate for this reconstruction. Shepp and Logan (1974) have also shown a significant noise suppression of 6 db in the reconstruction using a spatial average (3-point weighting average) with the convolution technique.

Direct Matrix Method. Iteration procedures are designed to minimize the square of the weighted differences between the observed data and the expected distribution of events with a given concentration of radionuclide,

$$\tilde{R}(A) = \sum_{k,\theta} \left[\frac{P_{k\theta} - R_{k\theta}(A)}{\sigma_{k\theta}} \right]^2 \tag{34}$$

where $P_{k\theta}$ is the measured projection,

$\sigma^2_{k\theta}$ is the variance in P_k

$R_{k\theta}(A)$ is the expected projection for concentration A.

$R_{k\theta}(A)$ is a linear function of A and can be written as

$$R_{k\theta}(A) = \sum_i A_i F_i^{k\theta} \tag{35}$$

where i sums over pixels. Representing k and θ by the single index j we get,

$$R_j(A) = FA = \sum_i F_{ji} A_i \ , \tag{36}$$

$$\tilde{R}(A) = \sum_j \left[\frac{P_j - R_j}{\sigma_j} \right]^2 = \sum_j \left[\frac{P_j - \sum_i F_{ji} A_i}{\sigma_j} \right]^2 \tag{37}$$

This can be written in vector notation as follows,

$$\tilde{R}(A) = (P - FA)^T \Phi^{-1} (P - FA)$$

where Φ^{-1} is the inverse of the covariance matrix in the measured projections P and is diagonal since the measured projections are assumed independent. $\tilde{R}(A)$ is minimized when

$$F^T \Phi^{-1} FA = F^T \Phi^{-1} P , \tag{38}$$

or

$$A = (F^T \Phi^{-1} F)^{-1} F^T \Phi^{-1} P \tag{39}$$

Another unbaised estimator is obtained by substituting unity for the variance of the measured values P, namely

$$A = (F^T F)^{-1} F^T P . \tag{40}$$

With good statistics, the results from these two estimators will be close.

For a given experimental situation (i.e., a fixed number of angles and fixed field of view) the matrix F is fixed, independent of the distribution of radionuclide under study. The vector $F^T P$ (usually called the back projection) is the convolution of the source by an appropriate function (1/r for an infinity of rotation angles). $F^T F$ represents this convolution.

Then, given the back projection of a certain distribution of radionuclide, one can envision operating on it with the precalculated matrix $(F^T F)^{-1}$ to obtain the reconstruction. In fact, $F^T F$ has very large dimensions, and calculating its inverse on the largest computers does not seem feasible at this time. (For a 64 × 64 array of pixels, $F^T F$ has dimensions of 4096 × 4096). We intend to investigate the possibility of calculating an approximation to the matrix $(F^T F)^{-1}$.

For continuous rotation angles F^TF falls off as $1/r$, and it is expected that the inverse $(F^TF)^{-1}$ also falls off as the distance between pixels increases. Therefore, we intend to explore the use of an approximation to $(F^TF)^{-1}$ which is also a convolution, but whose elements are zero for pixels separated by some minimum distance. This procedure has been tried on various phantoms with results which compare favorably with the iterative least squares technique.

Marr's Positron Technique. Another technique we are considering was proposed by Marr (1974). For N detectors, the number of coincidence lines of position is N(N-1)/2. This value includes near neighbor detector combinations, which in practice would not be used. These projection sample points are represented by

$$\{g(I,J) \mid 1 \leqslant I \leqslant N,\ 1 \leqslant J \leqslant N - 1\}$$

where I and J refer to detectors. Note that g(I,I) cannot be a data sample point since a detector cannot record a coincidence with itself. The reconstructed image $\rho(x,y)$ for this data set is given by the following equations

$$\rho(x,y) = \sum_{n=0}^{M} \sum_{k=0}^{[(M-n)/2]} (\alpha_{n,k} \sin n\psi + \beta_{nk} \cos n\psi) r^n Q_{n,k}(r^2) \qquad (41)$$

$$\begin{pmatrix} x = r\cos\psi \\ y = r\sin\psi \end{pmatrix}$$

where

$$\beta_{0,k} = \frac{2k+1}{N^2} \sum_{I,J} \sin\left[(2k+1)\frac{\pi J}{N}\right] g(I,J) \ . \ . \ . \ 0 \leqslant k \leqslant \frac{N-2}{2} \ , \qquad (42)$$

$$\begin{Bmatrix} \alpha_{n,k} \\ \beta_{n,k} \end{Bmatrix} = \frac{2(n+2\ k+1)}{N^2} \sum_{I,J} \sin\left[(n+2\ k+1)\frac{\pi J}{N}\right] \times \begin{Bmatrix} \sin \\ \cos \end{Bmatrix} \left[\frac{n\pi}{N}(2I+J-2)\right] g(I,J) \qquad (43)$$

$$. \ . \ . \ 1 \leqslant n \leqslant N - 2,\ 0 \leqslant k \leqslant \left[\frac{N-n-2}{2}\right],$$

$$Q_{n,k}(t) = \frac{1}{k!\ t^n} \frac{d^t}{dk^t} \{t^{n+k}(t - 1)^k\} , \tag{44}$$

and where M is some specified value such that $M \leqslant N - 2$. The Radon transform of $\rho(x,y)$ fits the data in a least squares sense.

7. RUBIDIUM GENERATOR AND DOSE

Two ^{82}Rb generators have been fabricated with about 1 mCi of ^{82}Sr produced at the Lawrence Berkeley Laboratory 88-inch cyclotron using the reaction $^{85}Rb(p,4n)^{82}Sr$ (Yano and Anger, 1968). A ^{82}Rb generator with 6 mCi capacity can be prepared using the same principles of eluting ^{82}Rb from a weakly acidic cation exchange resin. The eluant is 10-30 cc of 2-3% NaCl. Experience has shown that we have only 10^{-5} contamination from ^{82}Sr.

The total body dose is approximately 10 mrads for 6 mCi ^{82}Rb. This dose is in good part due to the energetic positrons. The positron dose (in rads) is calculated from:

$$\text{Dose } \beta^+ = 73.8\ C_0\ T_{\frac{1}{2}} \int_0^{E_{max}} N(E)\ E\ dE \qquad (45)$$

where C_0 is the concentration in tissue (μCi/gm) immediately after injection; assuming an equal distribution, i.e., 6000 microcuries, 70,000 gms. $T_{\frac{1}{2}}$ is the half life in days, and N(E) is the density distribution for positrons of energy E. For ^{82}Rb this integral is 1.4 MeV. The half life in days is 8.68×10^{-4}. Thus the positron dose is 8 millirads.

The gamma ray dose is calculated from the absorbed fraction method introduced by G. Brownell and gives only one fourth the dose given from the positrons. Thus the total dose is 10 millirads for a 6 millicurie injection.

TABLE 1.

CARDIAC IMAGING

Photoscanning by rectilinear scanner or imaging with the gamma camera.

Isotope	Limitations	Investigators
^{131}Cs	Low energy (29.4) Xe x-rays absorbed by photoelectric process in ribs and sternum. Long half-life.	Carr et al., 1964 Bing, 1967 Collier et al., 1968
^{129}Cs or ^{43}K	High whole-body dose per amount injected and limitation in resolution due to 375 keV photons. Expense of isotope. High dose, high energy and high cost.	Yano et al., 1970 Romhilt et al., 1973 Smith et al., 1970 Bennett et al., 1972
^{134m}Cs	Short half-life relative to optimum scanning time and availability.	Chandra et al., 1973
^{43}K	High energy photons (620, 373) and high cost. Rapid heart clearance.	Holman et al., 1973a Hurley et al., 1971 Zaret et al., 1973 Strauss et al., 1973 Ishii et al., 1973 Smith et al., 1972 Botti et al., 1973 MacIntyre et al., 1972 Poe, 1972
$^{13}NH_3$ (gamma)	High energy gammas (511 keV) from positron annihilation leads to low resolution because of difficulties in collimation. Need for cyclotron nearby.	Harper et al., 1972 Monohan et al., 1972

Table 1. Cardiac Imaging (continued)

Isotope	Limitations	Investigators
$^{13}NH_3$ (positron)	Need for positron camera and hospital cyclotron.	Hoop et al., 1973
^{81}Rb	High energy (450-520) leads to low resolution due to difficulty in collimation.	Budinger et al., 1973 Martin et al., 1974
^{82}Rb (positron)	Requires positron camera of high count rate capacity for studies in man.	Yano and Anger, 1968 Budinger et al., 1974
^{201}Thallium	Relative to other isotopes limitation is long half-life, 75 hrs., obviating repeated studies. Compares well in other respects.	Lebowitz et al., 1973
^{131}Ifatty acids	Availability and statistics. Low statistics per patient dose.	Bonte et al., 1973 Poe et al., 1973
^{99m}Tc-tetracycline	Unavailability of radiopharmaceutical with sufficient activity. Accumulates in fresh infarcts only 3-7 days.	Holman et al., 1973b Cook et al., 1974
^{99m}Tc-pyrophosphate		Bonte et al., 1974
Coronary Injection		
^{43}K	Invasive, see ^{43}K above.	Holman et al., 1973a
Microspheres ^{131}I, ^{99m}Tc	Invasive.	Ashburn et al., 1971 Weller et al., 1972 Jansen et al., 1973
Xe	Invasive.	Cannon et al., 1973 Pachinger et al., 1973

Table 1. Cardiac Imaging (continued)

Isotope	Limitations	Investigators
Precordial Counting		
Use of NaI(T) probe or positron coincidence systems.		
^{42}K, ^{86}Rb	No or limited spatial resolution capabilities. Variable and unknown background contribution.	Love et al., 1954 Love et al., 1957 Donato et al., 1964
^{84}Rb (positron)	No or limited spatial resolution.	Levi and DeOliveira, 1961 Bing et al., 1964 Cohen et al., 1965 Luebs et al., 1966 Cohen et al., 1967 McHenry et al., 1967 Teb et al., 1969

TABLE 2.

PRELIMINARY SPECIFICATIONS

1. Physical

External Ring Diameter	170 cm
Crystal Ring Diameter	80 cm
Minimum Lead Collimator Diameter	40 cm
Crystal Size	0.8cm×3cm×5cm
Total Number of Crystals	288
Sections	8
Crystals per Section	36
Photomultiplier Tubes per Section	9
Total Number of PMTs	72
Crystals in Coincidence with Opposite	62
Effective Diameter of Full Sensitivity	~ 30 cm
Weight of Ring Assembly and Shield	600 kg

2. Performance:

Resolution at Center	6mm FWHM
Slice Thickness at Center	5 to 15mm FWHM
Pulse Pair Resolving Time	10^{-8} sec

TABLE 3.

PROPERTIES OF A RING DETECTOR SYSTEM[a]
FOR THREE ASSUMED ENERGY RESOLUTIONS

Quantity	Symbol	Units	Case I	Case II	Case III
Energy resolution (FWHM) at 511 keV	Γ	%	none	30	15
Energy threshold	E_p	keV	100	410[b,c]	460[b,c]
Approximate maximum scattering angle corresponding to E_p (Eq. 13)	θ_p	degrees	180	41	27
Effective maximum scattering angle	θ_p	degrees	40	40	27
Minimum scattered gamma energy corresponding to θ_m (Eq. 14)	E_m	keV	415	415	460
Average detection efficiency for gamma ray energies from E_m to 511 keV	ε_m	%	65	25	25
Detection efficiency for 511 keV gammas	ε	%	50	20	20
Probability that a 511 keV gamma ray will scatter and retain an energy above E_p (Eq. 24)	P_p	%	63	20	10
Average detection efficiency for gamma ray energies from E_p to 511 keV	ε_p	%	80	25	25
Geometry factor - one gamma scatters (Eq. 16)	g_1	--	0.31	0.31	0.23
Geometry factor - both gammas scatter (Eq. 19)	g_2	--	0.19	0.19	0.13
Rate for unscattered coincident events (Eq. 5)	C_o	events per sec	6260	1000	1000
Sensitivity	C_o/ρ	events per sec per [μCi/cm]	31	5	5

Table 3. Properties of a ring detector system for three assumed energy resolutions (continued)

Quantity	Symbol	Units	Case I	Case II	Case III
Coincidence rate for one gamma scatter (Eq. 15)	C_1	events per sec	1735	267	198
Coincidence rate for two gamma scatter (Eq. 18)	C_2	events per sec	1190	176	120
Singles rate for entire ring (Eq. 23)	C_s	10^5 events per sec	10.2	1.83	1.46
Accidental coincidence rate for entire ring (Eq. 29)	C_a	events per sec	2290	74	47
Total event rate ($C_o + C_1 + C_2 + C_a$)		events per sec	11475	1517	1365
Background fraction $\frac{C_1+C_2+C_a}{C_o+C_1+C_2+C_a}$		%	45	34	27
Paralyzing deadtime	t_p	nsec	200	800	800
Fraction of events lost due to deadtime[c] (Eq. 32)	f_e	%	5	23	23

[a]Physical specifications of assumed ring detector system are as follows:

c = detector ring radius = 40 cm

S = shielding slit width = 2 cm

T = shielding slit depth = 20 cm

P_s = probability of scattering on energing from the center of a 20 cm diam cylinder of water = 63%

f = 0.22 (for 288 crystals, each would be in coincidence with the opposing 62 crystals)

θ_f = 40° maximum scattering angle imposed by coincidence requirement (approximate)

Table 3. Properties of a ring detector system for three assumed energy resolutions (continued)

[a](continued)

ρ = activity density = 200 μCi per axial cm

t = time resolution = 20 nsec

dimension of crystals along gamma line of flight = 5 cm

dimension of crystals along ring axis = 3 cm

dimension of crystals transverse to ring axis = 0.8 cm

R = radius of uniform geometrical sensitivity = 14 cm

G = gross singles rate per segment = 1.3×10^5 counts per sec

[b]Corresponds to a 7% photopeak loss, assuming that the photopeak has a Gaussian distribution.

[c]This event loss has not been included elsewhere in this table.

TABLE 4.

THE GEOMETRICAL FACTORS g_1 AND g_2
AS A FUNCTION OF THE MAXIMUM EFFECTIVE SCATTERING ANGLE θ_m

θ_m	g_1	g_2
0°	0	0
10°	0.10	0.05
20°	0.18	0.10
30°	0.26	0.15
40°	0.31	0.19
50°	0.36	0.23
60°	0.40	0.26

REFERENCES

This work was done with support from the U.S. Energy Research and Development Administration.

Alvarez, L.W.: Hodoscope design to minimize photomultiplier use; Rev. Sci. Instr. 31, 76 (1960).

Anger, H.O.: Survey of radioisotope cameras; ISA Trans. 5, 311 (1966).

Anger, H.O.: Tomographic gamma-ray scanner with simultaneous readout of several planes. In Fundamental problems in scanning, Charles C. Thomas, ed., 1968, p. 195, Springfield, Illinois.

Ansari, A.N., Atkins, H.L., Christman, D.R., Fowler, J.S., Karlstrom, K., MacGregor, R.R., Bradley-Moore, P.R., Wolf, A.P.: C-norepinephrine as a potential myocardial scanning agent; J. Nucl. Med. 14, 619, 1973.

Ashburn, W.L., Braunwald, E., Simon, A. et al.: Myocardial perfusion imaging with radioactive-labeled particles injected directly into the coronary circulation of patients with coronary artery disease; Circulation 44, 851-865 (1971).

Barrett, H.H., DeMeester, et al.: Tomographic imaging with a Fresnel zone-plate system. In Tomographic imaging in nuclear medicine Freeman, G.S., ed., New York, Society of Nuclear Medicine, 1973, pp. 106-121.

Bennett, K.R., Smith, R.L., Lehan, P.H. et al.: Correlation of myocardial ^{42}K uptake with coronary arteriography; Radiology 102, 117-124 (1972).

Blatt, S.L. Mahieux, J., Kohler, D.: Elimination of pulse pileup distortion in nuclear radiation spectra. Nucl. Instr. Meth. 60, 221-230, 1968.

Bing, R.J., Bennish, A., Bluemchen, G. et al.: The determination of coronary flow equivalent with coincidence counting technique; Circulation 29, 833-846 (1964).

Bing, R.J.: Scanning of the heart; New York State Jour. of Med. 67, 1406-1410 (1967).

Bing, R.J., Cowan, C., Boettcher, D. et al.: A new method of measuring coronary blood flow in man; JAMA 205, 277-280 (1968).

Bonte, F.J., Graham, K.D., Moore, J.G.: Experimental myocardial imaging with 131-I-labeled oleic acid; Radiology 108, 195-196 (1973).

Bonte, F.J., Parkey, R.W., Graham, K.D., Moore, J., Stokely, E.M.: A new method for radionuclide imaging of myocardial infarcts; Radiology 110, 473-474 (1974).

Botti, R.E., MacIntyre, W.J., Pritchard, W.H.: Identification of ischemic area of left ventricle by visualization of ^{43}K myocardial deposition; Circulation 47, 486-492 (1973).

Braunsfurth, J., Körner, H.J., Zeitauflösungeigenschaften von NaJszintillatoren, Nucl. Instr. Meth. 34, 202-212, 1965.

Brownell, G.L., Sweet, W.H.: Localization of brain tumors; Nucleonics 11, 40-45 (1953).

Brownell, G.L., Burnham, C.A., Silensky, S. et al.: New developments in positron scintigraphy and the application of cyclotron-produced positron emitters; Proc. Symp. Med. Radioisotope Scintig., Salzburg, 1968, pp. 163-176.

Brownell, G.L., Burnham, C.A.: The MGH positron camera. In Tomographic imaging in nuclear medicine, Freeman, G.S., ed., New York, The Society of Nuclear Medicine, Inc. (1971) pp. 154-164.

Brownell, G.L., Burnham, C.A., Hoop, B., and Kazemi, H., Positron scintigraphy with short-lived cyclotron-produced radiopharmaceuticals and a multicrystal positron camera, Medical Radioisotope Scintigraphy, Monte Carlo, Oct. 1972, pp. 313-330.

Budinger, T.F., Gullberg, G.T.: Three-dimensional reconstruction in nuclear medicine by iterative least squares and Fourier transform techniques; IEEE Trans. on Nucl. Sci. NS-21, 2-20 (1974).

Budinger, T.F., Macdonald, B.; Reconstruction of the Fresnel-coded gamma camera images by digital computer, J. Nucl. Med. 16, 309-313, 1975.

Budinger, T.F., Yano, Y. and Hoop, B: A comparison of $^{82}Rb^{+}$ and $^{13}NH_3$ for myocardial imaging; J. Nucl. Med. 16, 429-431, 1975.

Budinger, T.F., Yano, Y., McRae, J.: Rubidium-81 used as a myocardial agent; Lawrence Berkeley Laboratory Report LBL-2157 (1973).

Budinger, T.F., Yano, Y., McRae, J.; Rubidium-81 used as a myocardium imaging agent; Gesellschaft für Nuklearmedizin, Athens, Greece, Sept. 1973. Stuttgart, F.K., Schattauer-Verlag 1974, Lawrence Berkeley Laboratory Report LBL-2157.

Budinger, T.F., McRae, J., Yano, Y., Myers, W.G.: Myocardial imaging with ^{81}Rb; J. Nucl. Med. 15, 480 (1974).

Budinger, T.F., Gullberg, G.T.: Three-dimensional reconstruction in nuclear medicine emission imaging. IEEE Trans. NS 21/3, 2-20 (1974).

Budinger, T.F.: Quantitative nuclear medicine imaging: application of computers to the gamma camera and whole-body scanner. In Recent Advances in Nuclear Medicine, Lawrence, J.H., ed., Grune & Stratton, Ch. 2 (1974).

Burnham, C.A. and Brownell, G.L.: A multi-cyrstal positron camera; IEEE Trans. Nucl. Sci. NS19/3, 201-205 (1972).

Cannon, P.J., Dell, R.B., and Dwyer Jr., E.M.: Measurement of regional myocardial perfusion in man with ^{133}xenon and a scintillation camera; J. Clin. Invest. 51, 964-977 (1972).

Carr Jr., E.A., Gleason, G., Shaw, J. et al.: The direct diagnosis of myocardial infarction by photoscanning after administration of Cesium-131; Am. Heart J. 68, 627-636 (1964).

Chandra, R., Braunstein, P., Streuli, F. et al.: ^{134m}Cs, a new myocardial imaging agent; J. Nucl. Med. 14, 243-245 (1973).

Chang, L-T, Kaplan, S., Macdonald, B., Perez-Mendez, V., Shiraishi, L.: A method of tomographic imaging using a multiple pinhole coded aperture; Lawrence Berkeley Laboratory Report LBL-3001 (1974).

Cho, Z.H., Chan, J.K., Ericksson, L., Singh, M., Graham, S., Mac Donald, N.S. Yano, Y.; Positron ranges obtained for biomedically important positron-emitting radionuclides, J. Nucl. Med. 16, 1174-1176, 1975.

Cho, Z.H., Eriksson, L., Chan, J.: A circular ring transverse axial positron camera. In Workshop on Reconstruction Tomography in Diagnostic Radiology and Nuclear Medicine, Puerto Rico, April, 1975.

Chesler, D.A.: Positron tomography and three dimensional reconstruction techniques. In Tomographic Imaging in Nuclear Medicine, Friedman, G.S., ed., New York, Society of Nuclear Medicine (1973), pp. 176-183.

Cohen, A., Gallagher, J., Luebs, E.D. et al.: The quantitative determination of coronary flow with a positron emitter (rubidium-84); Circulation 32, 636-649 (1965).

Cohen, A., Zaleski, E., Luebs, E.D., et al.: The use of a positron emitter in the determination of coronary blood flow in man; J. Nucl. Med. 6, 651-666 (1965).

Cohen, A., Zaleski, E.J., Baleiron, H. et al.: Measurement of coronary blood flow using rubidium-84 and the coincidence counting method, a critical analysis; Am. J. Cardiol. 19, 556-562 (1967).

Collier, R.E., Matson, J.L., Tomme, J.W., et al.: Correlation of myocardial photoscanning and coronary angiography in angina pectoris; Radiology 91, 310-314 (1968).

Colombino, P., Fiscella, B., and Trossi, L., Nuovo Cimento 38, 707 (1965).

Cook, G.A., Holman, B.L., Westmoreland, N., et al.: Localization, detection and sizing of myocardial infarction with technetium-99m-tetracycline and electrophysiologic techniques; Am. J. Cardiol. 33, 131 (1974).

Derenzo, S., A comparison of two bi-planar positron cameras, LBL Group A Physics Note No. 804 (Dec. 1975).

Garwin, R.L.: Rev. Sci. Instr. 23, 755 (1952).

Gatti, A.E., Svelto, V.: Nucl. Instr. Meth. 43, 248 (1966).

Goldstein, H., Wilkins, J.E., Jr.: Calculations of the penetration of gamma rays; USAEC Report No. NYO-3075 (1954).

Gray, D.E. (ed.): American Institute of Physics Handbook, 3rd edition, McGraw-Hill, New York, 1972.

Grenier, R.P., Bender, M.A., Jones, R.H.: A computerized multi-crystal scintillation gamma camera. In Instrumentation in Nuclear Medicine, Vol. 2, Hine, G.J. and Sorenson, J.A. (eds.) Academic Press, New York, 1974.

Gunton, R.W., Evans, J.R., Baker, R.G., Spears, J.C., Beanlands, D.S.: Demonstration of myocardial infarction by photoscans of the heart in man; Amer. J. Cardiol. 16, 482-487 (1965).

Harper, P.V., Lathrop, K.A., Krizek, H., et al.: Clinical feasibility of myocardial imaging with $^{13}NH_3$; J. Nucl. Med. 13, 278-280 (1972).

Holman, B.L., Eldh, P., Adams, D.F., et al.: Evaluation of myocardial perfusion after intracoronary injection of radiopotassium; J. Nucl. Med. 14, 274-278 (1973a).

Holman, B.L., Dewanjee, M.K., Idoine, J., Fliegel, C.P., Davis, M.A., Treves, S., Eldh, P.: Detection and localization of experimental myocardial infarction with 99m Tc-tetracycline; J. Nucl. Med. 14, 595-599 (1973b).

Hoop, B., Jr., Smith, T.W., Burnham, C.A., et al.: Myocardial imaging with $^{13}NH_4^+$ and a multicrystal positron camera; J. Nucl. Med. 14, 181-183 (1973).

Hubbell, J.H.: Photon cross sections, attenuation coefficients, and energy absorption coefficients from 10 keV to 100 GeV, U.S. Natl. Bur. Stand. Report NSRDS-NBS 29, 1969.

Hurley, P.J., Cooper, M., Reba, R.C., Poggenburg, K.J., and Wagner, H.N.: ^{43}KCl, a new radiopharmaceutical for imaging the heart; J. Nucl. Med. 12, 516-519 (1971).

Ishii, Y., MacIntyre, W.J., Pritchard, W.H., et al.: Measurement of total myocardial blood flow in dogs with ^{43}K and the scintillation camera; Circ. Res. 33, 113-122 (1973).

Johnson, S.A., Robb, R.A., Greenleaf, J.F., Ritman, E.L., Lee, S.L., Herman, G.T., Sturn, R.E., Wood, E.H.: The problem of accurate measurement of left ventricular shape and dimensions from multi-plane roentgenographic data; Eur. J. Cardiol. 1, 241-258 (1974).

Jones, T. Brownell, G.L., Ter-Pogossian M.M.; "Equilibrium" images of shortlived radiopharmaceuticals for dynamic observations; J. Nucl. Med. 15, 505 (1974).

Kawana, M., Kyzek, H., Porter, J., Lathrop, K., Charleston, D., Harper, P.V.: Use of ^{199}Tl as a potassium analog in scanning; J. Nucl. Med. 11, 333 (1970).

Kuhl, D.E., Edwards, R.Q.: Image separation radioisotope scanning; Radiology 80, 653-661 (1963).

Kuhl, D.E., Edwards, R.Q.: Reorganizing data from transverse section scans of the brain using digital processing; Radiology 91, 975-983 (1968).

Kuhl, D.E., Edwards, R.Q., Ricci, A.R., Reivich, M.: Quantitative section scanning using orthogonal tangent correction; J. Nucl. Med. 14, 196-200 (1973).

Leb, G., Derntl, F., Goldschlager, N., et al.: Determination of effective and total coronary blood flow using Rb-84. Am. J. Med. Sci. 257, 203-217 (1969).

Lebowitz, E., Greene, M.W., Bradley-Moore, P.R., Atkins, H., Ansari, A., Richards, P., Belgrave, E.: Development and investigation of thallium-201 for medical use; J. Nucl. Med. (in press).

Lim, C.B., Chu, D., Kaufman, L., Perez-Mendez, V., Sperinde, J.: Characteristics of multiwire proportional chambers for positron imaging; IEEE Trans 21(1), 85 (1973).

Lim, C.B., Chu, D., Kaufman, L. et al.: Initial characterization of a multiwire proportional chamber positron camera, IEEE Trans. NS-22(1): 388-394, 1975.

Love, W.D. and Burch, G.E.: A study in dogs of methods suitable for estimating the rate of myocardial uptake of ^{86}Rb in man, and the effect of L-norepinephrine and pitressin on ^{86}Rb uptake; J. Clin. Invest. 36, 468-478 (1957).

Love, W.D., Ishikara, Y., Lyon, L.D. et al.: Differences in the relationships between coronary blood flow and myocardial clearance of isotopes of potassium, rubidium and cesium; Amer. Heart J. 76, 353-355 (1968).

Luebs, E.D., Cohen, A., Zaleski, E., et al.: The effect of nitroglycerine intensain, isoptin and papaverine on coronary blood flow in man measured by the coincidence counting technic and rubidium-84; Amer. J. Cardiol. 17, 535-541 (1966).

Marr, R.B.: On the reconstruction of a function on a circular domain from a sampling of its line integrals; J. Math. Anal. Appl. 45, 357-374 (1974).

Martin, N.D., Zaret, B.L., McGowan, R.L., et al.: Rubidium-81: A new myocardial scanning agent. Noninvasive regional myocardial perfusion scans at rest and exercise and comparison with potassium-43; Radiology 111, 651-656 (1974).

Mathews, C.M.E.: Comparison of coincidence counting and focusing collimators with various isotopes in brain tumor detection. Brit. J. Radiol. 37, 531 (1964).

Mathieu, L, Budinger, T.F.: Pinhole digital tomography; First World Congress of Nuclear Medicine, Tokyo, 1974.

McHenry, P.L., Knoebel, S.B.: Measurement of coronary blood flow by coincidence counting and a bolus of ^{84}Rb-Cl; J. Appl. Physiol. 22, 495-500 (1967).

Monahan, W.G., Tilbury, R.S., Laughlin, J.S.: Uptake of ^{13}N-labeled ammonia; J. Nucl. Med. 13, 274-277 (1972).

Muehllehner, G.: Positron camera with extended counting rate capability, J. Nucl. Med. 16, 653-657 (1975).

Pachinger, O.M., Tillmanns, H.H., Bing, R.J.: Coronary blood flow assessment with xenon and rubidium; Seminars in Nucl. Med. 3; 131-138 (1973).

Phelps, M.E., Hoffman, E.J., Mullani, N.A., et al.: Application of annihilation coincidence detection to transaxial reconstruction tomography; J. Nucl. Med. 16, 210-224 (1975).

Poe, N.D.: Comparative myocardial uptake and clearance characteristics of potassium and cesium; J. Nucl. Med. 13, 557-560 (1972).

Poe, N.D.: Comparative myocardial distribution patterns after intracoronary injection of cesium and labeled particles; Radiology 106, 341-346 (1973).

Poe, N.D., Robinson, G.D., MacDonald, N.S.: Myocardial extraction of variously labeled fatty acids and carboxylates; J. Nucl. Med. 14, 440 (1973).

Robb, R.A., et al.: Three-dimensional visualization of the intact thorax and contents: a technique for cross-sectional reconstruction from multiplanar x-ray views; Computers and Biomedical Research 7, 001-025 (1974).

Robertson, J.S., Marr, R.B., Rosenbaum, M., et al.: Thirty-two crystal positron transverse section detector; In Tomographic Imaging in Nuclear Medicine, Friedman, G.S., ed., New York, Society of Nuclear Medicine (1973), pp. 142-153.

Romhilt, D.W., Adolph, R.J., Sodd, V.J., et al.: Cesium-129 myocardial scintigraphy to detect myocardial infarction; Circulation 48, 1242-1251 (1973).

Sapirstein, L.A.: Fractionation of the cardiac output of rats with isotopic potassium; Circ. Res. 6, 689 (1956).

Sapirstein, L.A.: Regional blood flow by fractional distribution of indicators; Amer. J. Physiol. 193, 161 (1958).

Shepp, L.A., Logan, B.F.: The Fourier reconstruction of a head section; IEEE Trans. Nucl. Sci. NS-21(3), 21-43 (1974).

Smith, R.O., Love, W.D., Lehan, P.H., et al.: Delayed coronary blood flow detected by computer analysis of serial scans; Amer. Heart J. 84, 670-677 (1972).

Stewart, A.T., Canad. J. Phys. 35, 168 (1957).

Strauss, H.W., Zaret, B.L., et al.: Noninvasive evaluation of regional myocardial perfusion with potassium-43; Radiology 108, 85-90 (1973).

Ter-Pogossian, M.M., Phelps, M.E., Hoffman, E.J., et al.: A positron-emission transaxial tomograph for nuclear imaging (PETT); Radiology 114, 89-98, 1975.

Tidd, J.L., Dabbs, J.R., Levine, N.: Scintillator handbook with emphasis on cesium iodide, NASA technical memorandum No. NASA TM-X-64741, April 1973, available from the National Technical Information Service, Springfield, VA 22151 (unpublished).

Tiemann, J.J., Engeler, W.E., Baertsch, R.D., Brown, D.M.: Intercell charge-transfer structures for signal processing' IEEE Trans. Electron Devices ED-21, 300-308 (1974).

Vokelman, J., Van Dyke, D., Yano, Y., et al.: Myocardial scanning with ^{82}Rb; University of California Lawrence Berkeley Laboratory report LBL 775 (1972) 8 pp.

Wrenn, F.W., Good, M.L., Handler, P.: The use of positron-emitting radioisotopes for the localization of brain tumors; Science 113, 525 (1951).

Yano, Y., Anger, H.O.: Visualization of heart and kidneys in animals with ultrashort-lived ^{82}Rb and the positron scintillation camera; J. Nucl. Med. 9, 412-415 (1968).

Yano, Y., Van Dyke, D., Budinger, T.F., Anger, H.O., Chu, P.: Myocardial uptake studies with 129-Cs and the scintillation camera; J. Nucl. Med. 11, 663-668 (1970).

Yipintsoi, T., Dobbs, W.A., Scanlon, P.D., et al.: Regional distribution of diffusible tracers and carbonized microspheres in the left ventricle of isolated dog hearts; Circ. Res. 33, 573-587 (1973).

Zaklad, H., Derenzo, S.E., Muller, R.A., Smadja, G., Smits, R.G., Alvarez, L.W.: A liquid xenon radioisotope camera; IEEE Trans. NS-19(3), 206 (1972).

Zaret, B.L., Stenson, R.E., Martin, N.D., et al.: Potassium-43 myocardial perfusion scanning for the noninvasive evaluation of patients with false-positive exercise tests; Circulation 48, 1234-1241 (1973).

Zaret, B.L., Strauss, H.W., Martin, N.D., et al.: Noninvasive regional myocardial perfusion with radioactive potassium. Study of patients at rest, with exercise and during angina pectoris; New Engl. J. Med. 288, 809-812 (1973).

Zaret, B.L., Martin, N.D., McGowan, R.L., et al.: Rest and exercise potassium-43 myocardial perfusion imaging for the noninvasive evaluation of aortocoronary bypass surgery; Circulation 49, 688-695 (1974).

FIGURE CAPTIONS

1. Transverse section tomography of the human myocardium, using ^{129}Cs and multiple views taken by a Scintillation Camera with parallel channel collimation.

2. Transverse section tomography of the myocardium of the dog, as per Fig. 1.

3. Gated single view of the myocardium using ^{81}Rb and a Scintillation Camera with pinhole.

4. Comparison of ^{82}Rb to ^{13}N-ammonia myocardial imaging in a dog.

5. NaI(Tl) crystal in 0.25 mm thick stainless steel package manufactured by Harshaw Chemicals. Dimensions are 9.5 mm × 9.5 mm × 38 mm.

6. Schematic showing patient positioned inside the detector ring.

7. Example of assembly of crystals (inside lead collimator) connected to light pipes and photomultiplier tubes (PMTs). Signals from PMTs are checked for validity of code (to insure that detection occurred in one crystal only) before energy selection.

8. Example showing coding scheme for 6 crystals and 4 photomultipliers. Expansion to 36 crystals requires 5 additional photomultipliers.

9. Schematic of coincidence coding for 6 segment example. Each crystal is required to be in time coincidence with a pre-selected number of opposing crystals.

10. Schematic showing detector circle, collimator and geometrical quantities used in Section 5.2

11. Axial response function - calculated coincident response for a fixed angle ϕ (see Fig. 10) as an off-axis positron source is moved parallel to the Z axis.

12. Axial response function (averaged over all gamma ray directions) for various distances to the center of the detector circle.

13. Schematic showing that for off-axis points the transaxial resolution depends on the gamma ray direction.

14. Schematic showing a portion of the detector ring and the geometrical variables used in Section 5.6.

15. Transaxial point spread function (averaged over all gamma ray directions) for various distances to the center of the detector ring.

16. FWHM of transaxial point spread function (averaged over all gamma ray directions) vs. the distance to the center of the detector circle.

17. Axial response functions (on axis sources) for co-linear coincident gamma ray pairs and for single gamma rays (or non-co-linear coincident pairs).

18. Illustration showing how Compton Scattering can contribute background to the coincident event rate. Although two photons are in time coincidence, they are not colinear and provide erroneous spatial information. Unscattered coincident events can arise only from region between the dashed lines.

19. Energy lost by a gamma ray during Compton scattering as a function of the gamma ray scattering angle.

20. Cross section per unit solid angle for the Compton scattering of 500 keV gamma rays as a function of the gamma ray scattering angle.

21. Comparison of four techniques for three-dimensional reconstruction — back projection, simultaneous iterative reconstruction, least-squares, and back projection of filtered projections (BPFP) — using lucite phantoms and ^{99m}Tc.

22. Least-squares technique reconstruction of a phantom consisting of the letters "L" "O" "V" and the discrepancy between the true image and the reconstruction.

This report was done with support from the United States Energy Research and Development Administration. Any conclusions or opinions expressed in this report represent solely those of the author(s) and not necessarily those of The Regents of the University of California, the Lawrence Berkeley Laboratory or the United States Energy Research and Development Administration.

TECHNICAL INFORMATION DIVISION
LAWRENCE BERKELEY LABORATORY
UNIVERSITY OF CALIFORNIA
BERKELEY, CALIFORNIA 94720